

**Numerical Analysis of Near-Surface Flow Beneath  
Small-Scale Wind Driven Water Waves**

By:

Xiao Xia Hu

The Department of  
Mechanical & Industrial Engineering

Presented in Partial Fulfillment of the Requirements  
For the Degree of Master of Applied Science at  
Concordia University  
Montreal, Québec, Canada

April 2007

© Xiaoxia Hu, 2007



Library and  
Archives Canada

Published Heritage  
Branch

395 Wellington Street  
Ottawa ON K1A 0N4  
Canada

Bibliothèque et  
Archives Canada

Direction du  
Patrimoine de l'édition

395, rue Wellington  
Ottawa ON K1A 0N4  
Canada

*Your file    Votre référence*  
*ISBN: 978-0-494-37774-1*  
*Our file    Notre référence*  
*ISBN: 978-0-494-37774-1*

**NOTICE:**

The author has granted a non-exclusive license allowing Library and Archives Canada to reproduce, publish, archive, preserve, conserve, communicate to the public by telecommunication or on the Internet, loan, distribute and sell theses worldwide, for commercial or non-commercial purposes, in microform, paper, electronic and/or any other formats.

The author retains copyright ownership and moral rights in this thesis. Neither the thesis nor substantial extracts from it may be printed or otherwise reproduced without the author's permission.

**AVIS:**

L'auteur a accordé une licence non exclusive permettant à la Bibliothèque et Archives Canada de reproduire, publier, archiver, sauvegarder, conserver, transmettre au public par télécommunication ou par l'Internet, prêter, distribuer et vendre des thèses partout dans le monde, à des fins commerciales ou autres, sur support microforme, papier, électronique et/ou autres formats.

L'auteur conserve la propriété du droit d'auteur et des droits moraux qui protègent cette thèse. Ni la thèse ni des extraits substantiels de celle-ci ne doivent être imprimés ou autrement reproduits sans son autorisation.

---

In compliance with the Canadian Privacy Act some supporting forms may have been removed from this thesis.

While these forms may be included in the document page count, their removal does not represent any loss of content from the thesis.

Conformément à la loi canadienne sur la protection de la vie privée, quelques formulaires secondaires ont été enlevés de cette thèse.

Bien que ces formulaires aient inclus dans la pagination, il n'y aura aucun contenu manquant.

  
**Canada**

# **Abstract**

## **Numerical Analysis of Near-Surface Flow Beneath Small-scale Wind-Driven Water Waves**

Xiaoxia Hu

Previous studies have shown that microscale wave breaking plays a significant role in the process of heat, gas, and energy exchange between water and air. In this research, the numerical analysis of near-surface flow beneath small-scale wind driven water waves were studied using the model which was validated by the experiment.

A gas model was developed in present study to estimate the effect of wind on the water waves. An experiment was conducted at a wind speed of  $4.4 \text{ m}\cdot\text{s}^{-1}$  to validate the numerical model used in the simulations. The results showed excellent agreement between numerical and experimental studies at the interface and greater water depths. The model also captured the logarithmic behavior of the mean streamwise velocity, which is consistent with previous studies.

The two-dimensional simulating results for both clean water surface and contaminated water surface are presented in terms of mean streamwise velocity, wave characteristic including RMS wave amplitude and dominate wavelength, and the structure of vorticity near water surface. Also, some preliminary results of three-dimensional numerical simulations are presented for both clean and contaminated water surface.

# Acknowledgement

I would like to give my sincere thanks to my supervisor Professor Ali Dolatabadi and Professor Kamran Siddiqui for their excellent and continuous guidance throughout this research. I deeply appreciate their trust and confidence in me, which gave me courage to achieve my goals. I would also like to give my sincere thanks to my colleague Shaikh N. for his help in the experiment and other colleagues in the CFD Lab of Concordia University, Qingsong Zhu, Arabzadeh S., Arzpeyma A., Movassa M., Sanderse B., Samareh B., Srivatsan V.R. They have helped me a lot in technical problems and in English.

Special thanks give to my husband and my dear daughter for their support and trust. Without their understanding, I could not have completed my research in time.

Finally, I would like to thank Simulent Inc., Toronto, Ontario for providing access to the SIMULENT code which is modified for the present study.

# Table of Contents

<b>LIST OF FIGURES.....</b>	<b>VIII</b>
<b>LIST OF TABLES.....</b>	<b>X</b>
<b>NOMENCLATURE .....</b>	<b>XII</b>
<b>CHAPTER I: INTRODUCTION.....</b>	<b>1</b>
1.1    LITERATURE REVIEW.....	3
1.1.1 WATER WAVES.....	3
1.1.1.1 MICROSCALE BREAKING WAVE.....	4
1.1.1.2 SURFACE CONTAMINATION.....	10
1.1.2 NUMERICAL STUDIES ON WATER WAVES.....	12
1.2    MOTIVATIONS.....	17
1.3    OBJECTIVE.....	18
1.4    THESIS ORGANIZATION.....	19
<b>CHAPTER II: METHODOLOGY.....</b>	<b>20</b>
2.1.    NUMERICAL STUDY .....	20
2.1.1 GOVERNING EQUATIONS.....	20
2.1.2 VOLUME AND FLUID METHOD.....	22
2.1.3 THE TWO-STEP PROFFECTION METHOD.....	23
2.1.4 MOMENTUM ADVECTION.....	25
2.1.5 VISCOSITY.....	30
2.1.6. THE GAS MODEL AND OTHER BOUNDARY CONDITIONS.....	32

2.1.7 TIMESTEP RESTRICTIONS.....	33
2.2. EXPERIMENTAL STUDY .....	34
2.2.1 EXPERIMENTAL SETUP AND INSTRUMENTATION.....	34
2.2.2 PIV TECHNIQUE.....	37
2.2.3 WAVE PROFILE MESUREMENTS.....	40
2.2.4 COMPUTATION OF INSTANTANEOUS VELOCITY FIELDS.....	42
2.2.5 COMPUTATION OF MEAN VELOCITY COMPONENTS.....	45
<b>CHAPTER III: MODEL VALIDATION.....</b>	<b>46</b>
3.1. GAS MODEL VALIDATION.....	46
3.2 EXPERIMENTAL VALIDATION.....	48
<b>CHAPTER IV: RESULTS AND DISCUSSIONS.....</b>	<b>53</b>
4.1. TWO-DIMENSIONAL SIMULATIONS.....	53
4.1.1 CLEAN SURFACE CONDITION.....	53
4.1.2 EFFECT OF SURFACE CONTAMINATION.....	59
4.2. THREE-DIMENSIONAL SIMULATIONS.....	65
4.2.1 CLEAN SURFACE CONDITION .....	67
4.2.2 EFFECT OF SURFACE CONTAMINATION ON WATER WAVES.....	73
<b>CHAPTER V: CONCLUSIONS AND RECOMMENDATION .....</b>	<b>78</b>
5.1. CONCLUSION.....	78
5.2 RECOMMENDATION FOR FUTURE RESEARCH.....	81
<b>REFERENCES .....</b>	<b>82</b>
<b>APPENDIX A .....</b>	<b>88</b>

# List of Figures

Figure 1.1 (Top) Conceptual model of a microscale breaking wave with bore-like crest preceded by capillary waves riding along the forward face. (Bottom) A digital video image of a microscale breaking wave with an approximate wavelength of 10 cm ...	5
Figure 1.2 The conceptual model of a disruption and recovery of the skin layer due to wave breaking .....	7
Figure 1.3 An IR image at a wind speed of $8.5 \text{ m}\cdot\text{s}^{-1}$ . The wake signatures produced due to the disruption of the cool skin layer by microscale breaking waves, are outlined in black. The dimensions of the IR image are $34.3\text{cm} \times 34.3\text{cm}$ .....	7
Figure 2.1 Volume fraction advection in 2D: (a) an exact liquid interface; (b) corresponding $f_{i,j,k}$ and the associated planar interface; (c) with $u$ positive, the shaded region to the right of the dashed line is advected into the neighboring cell. ....	23
Figure 2.2 A 2D view of cell $(i,j,k)$ . Velocities $u,v,w$ (normal to the page-not shown) are specified at the centre of cell faces, pressure $p$ and body force $F_b$ at the cell centre.....	24
Figure 2.3 (a) the x-component momentum control volume about the velocity $u_{i+\frac{1}{2},j,k}$ ; (b) the interpolated flux velocities at the control volume faces. ....	27
Figure 2.4 Shear stresses specified at the faces of an x-momentum control volume (note that the shear stresses related to $z$ direction are not shown here).....	31
Figure 2.5 Scheme of boundary conditions for the simulated tank.....	33
Figure 2.6 Schematic of the experimental tank.....	36
Figure 2.7 Schematic of the experimental setup and instrumentation in the wind-wave flume (not to scale).....	36
Figure 2.8 A schematics of a typical PIV system.....	38

Figure 2.9	Circuit diagram showing the timing of the laser pulses in an image pair. A pulse generator controls the timing and duration of each laser pulse.....	38
Figure 2.10	A typical PIV image at a wind speed of $4.4 \text{ m} \cdot \text{s}^{-1}$ (a) the original image; (b) after setting airside as background; (c) computed surface wave profile plotted as a white line.....	40
Figure 2.11	The two-dimensional instantaneous velocity field obtained by processing the PIV image in figure 2.10.....	44
Figure 3.1	A typical surface wave profile obtained from (a) numerical simulation; (b) experimental data.....	49
Figure 3.2	Frequency spectra computed from experimental wave profile data at a wind speed of $4.4 \text{ m} \cdot \text{s}^{-1}$ .....	50
Figure 3.3	Mean streamwise velocity profile at a wind speed of $4.4 \text{ m} \cdot \text{s}^{-1}$ (a) linear scale ;(b)semi-logarithmic scale. ( $Z=0$ represents the water surface).....	52
Figure 4.1	A typical field of velocity vectors obtained from (a) numerical simulation; (b) experimental data.....	54
Figure 4.2	A typical field of vorticity obtained from numerical simulation.....	55
Figure 4.3	Mean streamwise velocity profile obtained from numerical simulations for different wind speed.....	56
Figure 4.4	Semi-log mean streamwise velocity profile plotted in the form of the velocity defect law in wall coordinates.....	59
Figure 4.5	The mean streamwise velocity profiles for various wind speeds and surface tension. (a) wind speed $4.0 \text{ m} \cdot \text{s}^{-1}$ ; (b) wind speed $4.4 \text{ m} \cdot \text{s}^{-1}$ .....	61
Figure 4.6	Semi-log mean streamwise velocity profile plotted in the form of the velocity defect law in wall coordinates. ....	62
Figure 4.7	Vorticity distribution at a wind speed of $4.4 \text{ m} \cdot \text{s}^{-1}$ for various surface tension (a) $0.073 \text{ N} \cdot \text{m}^{-1}$ (clean surface); (b) $0.050 \text{ N} \cdot \text{m}^{-1}$ ; (c) $0.012 \text{ N} \cdot \text{m}^{-1}$ .....	64
Figure 4.8	An area of wind blown water surface $4\text{m} \times 3\text{m}$ , showing a small spilling breaker and a lot of microscale breaking.(Banner 1993).....	66
Figure 4.9	The wind-generated water waves conducted in a tank of $3\text{m} \times 0.45\text{m} \times 0.9\text{m}$ .....	66



Figure 4.10 Three-dimensional wave generation at a wind speed of $3.6 \text{ m}\cdot\text{s}^{-1}$ . (a) time = 0.26s; (b) time = 0.40s; (c) time = 0.50s; (d) time = 0.60s.....	68
Figure 4.11 Three-dimensional wave generation at a wind speed of $4.4 \text{ m}\cdot\text{s}^{-1}$ . (a) time = 0.2s; (b) time = 0.30s.....	71
Figure 4.12 Structure of vorticity for clean surface at a wind speed of $3.3 \text{ m}\cdot\text{s}^{-1}$ (a) spanwise-vorticity; (b) streamwise-vorticity.....	72
Figure 4.13 Three-dimensional wave generation at a wind speed of $3.6 \text{ m}\cdot\text{s}^{-1}$ and surface tension of $0.0228 \text{ N}\cdot\text{m}^{-1}$ (a) time = 0.50s; (b) time = 0.60s; (c) time = 0.70s.....	73
Figure 4.14 Structure of vorticity for contaminated water surface at a surface tension of $0.0228 \text{ N}\cdot\text{m}^{-1}$ and a wind speed of $3.6 \text{ m}\cdot\text{s}^{-1}$ (a) spanwise-vorticity; (b) streamwise-vorticity.....	76
Figure 4.15 Water surface profiles at a wind speed of $3.6 \text{ m}\cdot\text{s}^{-1}$ and surface tension of (a) $0.0723 \text{ N}\cdot\text{m}^{-1}$ (clean surface); (b) $0.050 \text{ N}\cdot\text{m}^{-1}$ ; (c) $0.025 \text{ N}\cdot\text{m}^{-1}$ .....	77

# List of Tables

Table 3.1	Friction velocity comparisons obtained from experimental data and the gas model (calculated by equation 2.30).....	46
Table 3.2	Wind velocity distribution near the water surface obtained from experimental data and the gas model estimated by equation 2.31.....	47
Table 3.3	Wave characteristics obtained from numerical and experimental results .....	51
Table 4.1	The mean streamwise velocities ( $\text{cm}\cdot\text{s}^{-1}$ ) corresponding to different depths and different wind speed.....	57
Table 4.2	The friction velocity $u_*$ at a function of wind speed.....	58
Table 4.3	Wave characteristics with different surface tension at a wind speed of $4.4 \text{ m}\cdot\text{s}^{-1}$ .....	63

# Nomenclature

$C$	Courant number
$f_d$	dominated wave frequency
$F$	volume fraction
$F_b$	body force
$\bar{g}$	gravity
$p$	pressure
$RMS$	root mean square
$t$	time
$T$	temperature
$u_*$	wall-friction velocity
$u, v, w$	velocity components in x,y,z-directions
$u^fl, v^fl, w^fl$	flux velocities in x,y,z-directions
$U_{gas}$	free stream gas velocity

$U^+$	defect velocity
$\vec{V}$	velocity vector
$\tilde{\vec{V}}$	a velocity field calculated from the incremental changes of $\vec{V}^n$ resulting from viscosity, advection, gravity and body forces

#### Greek symbols

$\alpha^{vl}$	Van Leer limiter
$\Delta x, \Delta y, \Delta z$	grid size in x, y, z direction
$\lambda_d$	dominated wavelength
$\mu$	dynamic viscosity
$\nu$	kinematic viscosity
$\rho$	density
$\tau$	viscous stress tensor

#### Subscripts

$a$	air
$f$	fluid
$min$	minimum value
$max$	maximum value

$s$  surface

*Superscripts*

$fl$  flux quantities

# Chapter I

## Introduction

The air-sea interface comprises approximately 70% of the Earth's surface, and the ocean-atmosphere interaction has a significant impact on the global climate. The energy transfer from the ocean drives atmospheric circulation, while at the same time, the ocean acquires energy and momentum from the atmospheric circulation i.e. the wind. The boundary layers on both sides of the interface control the transfer of heat and gas across the interface. When wind blows over the water surface, it produces surface waves of different wavelengths and amplitudes anywhere from a few millimeters to hundreds of meters. These waves alter the flow structure in both the airside and waterside boundary layers and thus influence the air-water transport processes. The occurrence of small-scale wind-generated waves is wide spread over the ocean surface. Previous studies have suggested that the cumulative effect of these small-scale waves on air-sea heat and mass transport could be significant (Melville 1996). Some recent studies have confirmed this hypothesis by showing that the near-surface flow field beneath wind-generated waves plays a very crucial role in controlling the gas and heat fluxes across the interface (Siddiqui *et al.* 2001, Zappa *et al.* 2001).

The breaking of surface waves plays an important role in air-sea interactions (Melville 1996). By generating near-surface turbulence, these breaking waves not only enhance the transfer of gas and heat across the air-sea interface, but also dissipate wave energy and generate ocean currents by transferring momentum from the wave field.

Breaking waves can be generated over a wide range of scales (lengths 0.1-100 m) and intensities (Rapp and Melville 1990). Large scale breaking waves refer to the waves with the entrainment of significant volumes of air. These kinds of waves can also produce a whitecap. The term of "Microscale Breaking" was introduced by Banner and Phillips (1974) in order to describe the breaking of very short gravity waves which usually occur at low to moderate wind speeds (i.e. 4-12 m·s<sup>-1</sup>). In microscale breaking, surface tension is strong enough to prevent air entrainment.

Previous studies have shown that microscale breaking may be very important in controlling the fluxes of heat, gas and momentum across the air-water interface (Melville 1996, Banner and Peregrine 1993, Phillips 1977). Gas exchange across the air-sea interface has significant effect on the bio-geochemical cycling of gases in our living environment. The correct prediction of oxygen transfer across the air-water interface is critical for modeling water quality (Emerson 1987, Chu and Jirka 1995). Banner and Peregrine (1993) also showed that accurate estimates of CO<sub>2</sub> transfer rate between the atmosphere and ocean are important for prediction of global warming. Ocean circulation models used to estimate the global ocean CO<sub>2</sub> uptake are very sensitive to the air-water CO<sub>2</sub> transfer velocity (Sarmiento *et al.* 1992). Therefore, it is necessary to better understand the processes that control air-sea gas transfer velocity to obtain accurate estimates of CO<sub>2</sub> flux.

It is well known that nearly all the ocean surfaces are covered with contaminated surfactants. Mass and Milgram (1998) concluded that most natural sea surfactant molecules have sufficient surface tension to form surface films over a wide range of ocean surface. Previous studies have already shown that the existence of surfactant films

has a significant effect on the gas, heat, and energy transfer between air and sea. The effect on the gas transfer, especially  $\text{CO}_2$  and  $\text{O}_2$  has an important meaning in the study of our ecosystem.

The flow field beneath wind waves is complex due to the presence of three components of velocity namely mean, wave and turbulent, and their interactions. The experimental investigations in the near-surface region beneath wind waves are challenging due to the fluctuation of the water surface and the complexity of the turbulent flow in this region. The numerical investigations are also difficult due to the three-dimensional nature of the flow and air-water flow interactions. Until now, few numerical investigations have been conducted on small-scale wind driven water waves.

## **1.1 Literature Review**

### **1.1.1 Water Waves**

Water waves refer to the motion of unsteady free surface subjected to gravitational forces. In terms of the effects of surface tension, water waves can be divided into three categories: capillary waves, capillary-gravity waves and gravity waves. A capillary wave is dominated only by the effects of surface tension, whose wavelength is usually no more than one centimeter. However, for a capillary-gravity wave, both the gravitational force and the surface tension play an important role in the generation and propagation of the wave, and for a gravity wave, the effect of surface tension can be ignored and only the effect of gravity is required to be considered. Ocean waves and tsunamis are typical examples of gravity waves. Wind waves, as the most important kind of water waves, refer to the waves at the water surface of the ocean generated by wind. They are also



called wind-generated waves. Wind waves, the most ever-present oceanic feature, are generated by the friction between water and air and driving force of the wind.

The problem of water waves, as one of the oldest topics in fluid mechanics and hydrodynamics, has been studied over the past several decades. The traditional interest in water waves is due to their importance in the design of ships and near-shore structures. More recent interest is due to the need to understand tsunamis, energy and mass exchange processes at the air-sea interface, the generation and detection of internal waves by submarines, the scattering of radar by capillary waves, the design of off-shore structures such as oil rigs, and sediment transport and beach erosion due to normal as well as storm seas. Just as any other area of mechanics, fundamental techniques or knowledge generated for one application can be easily carried over to other areas. The better understanding of water waves are helpful in the problems involving film coating processes, fuel sprays, droplet and bubble dynamics or stability, and cavitations.

#### **1.1.1.1 Microscale Breaking Waves**

Wave breaking is an irregular or random process in space and time and it is a highly nonlinear phenomenon (Chen *et al.* 1999). It can be generated over a wide range of scales (lengths 0.1-100 m) and intensities (Rapp and Melville 1990). Large scale breaking waves refer to the waves with significant entrainment of air. These kinds of waves can also produce a whitecap. The term of microscale breaking was introduced by Banner and Phillips (1974) to describe the breaking of very short gravity waves without air entrainment. In microscale breaking waves, surface tension is strong enough to prevent air entrainment. Microscale wave breaking usually occurs at low to moderate wind speeds (i.e.  $4\text{-}12\text{m}\cdot\text{s}^{-1}$ ) and is in the order of 0.1 to 0.5m in length and a few centimeters

in amplitude. They have a bore-like crest directly preceded by parasitic capillary waves riding along forward face (Jessup *et al.* 1997). Figure 1.1 is a typical example of microscale breaking.

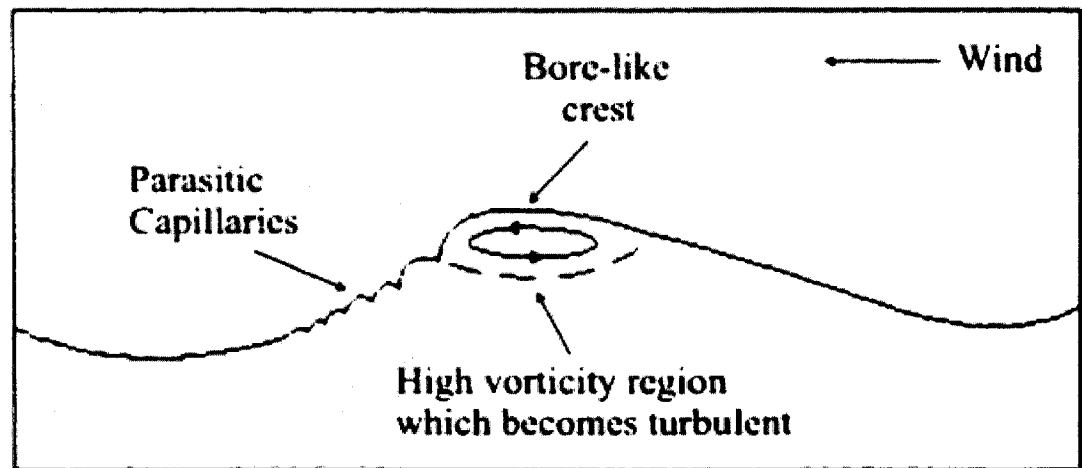


**Figure 1.1** (Top) Conceptual model of a microscale breaking wave with bore-like crest preceded by capillary waves riding along the forward face. (Bottom) A digital video image of a microscale breaking wave with an approximate wavelength of 10 cm (Jessup *et al.* 1997).

Microscale breaking may include many complex processes such as nonlinear deformation of the laminar flow during steepening, generation of vorticity at the water surface and rapid generation of turbulence (Duncan 2001). Moreover, the physical

mechanisms that lead to microscale wave breaking are not well understood. Since microscale breaking is without air entrainment, it is difficult to use standard optical techniques to measure microscale breaking. Jessup *et al.* (1997) put forward a new method using infrared (IR) imagery to detect microscale breaking waves. It is shown that microscale breaking waves produce thermal surface signatures that can be quantified by infrared imaging techniques. The temperature of the ocean surface is a few tenths of a degree Celsius cooler than the bulk water temperature immediately below. The turbulence generated by microscale breaking waves destroys this cool skin layer and brings warmer bulk water to the surface, producing a warm thermal wake at the surface which can be detected by IR imagery. This cool skin layer recovers as the wake dissipates. Figure 1.2 is the conceptual model of the disruption and recovery of the skin layer due to wave breaking as described by Jessup *et al.* 1997. A typical infrared image of the water surface at a wind speed of  $8.1\text{m}\cdot\text{s}^{-1}$  is shown in Figure 1.3. Surface signatures due to the disruptions of the cool skin layer by microscale breaking waves can also be clearly seen and are outlined in black.

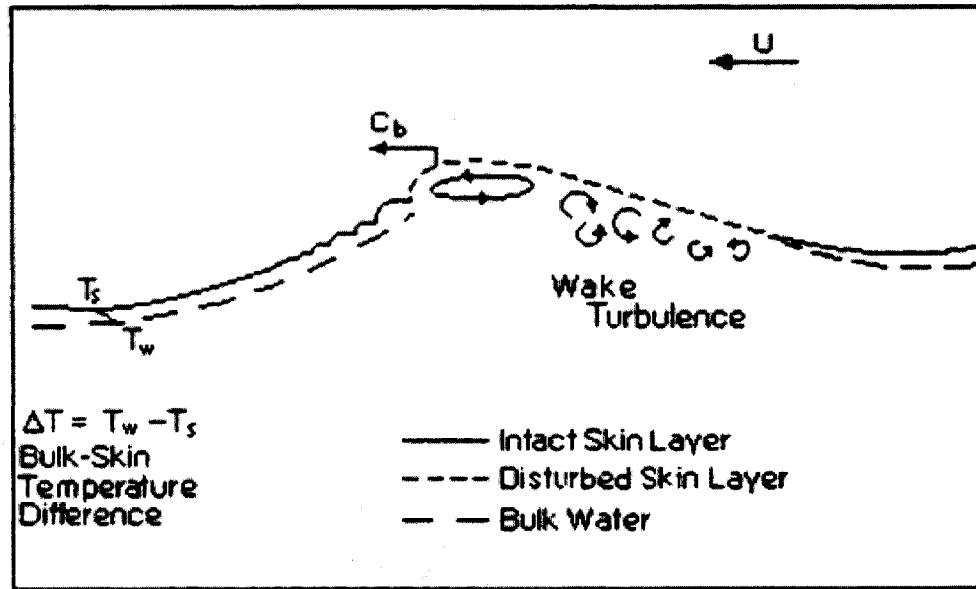


**Figure 1.2** The conceptual model of a disruption and recovery of the skin layer due to wave breaking (Jessup et al. 1997)

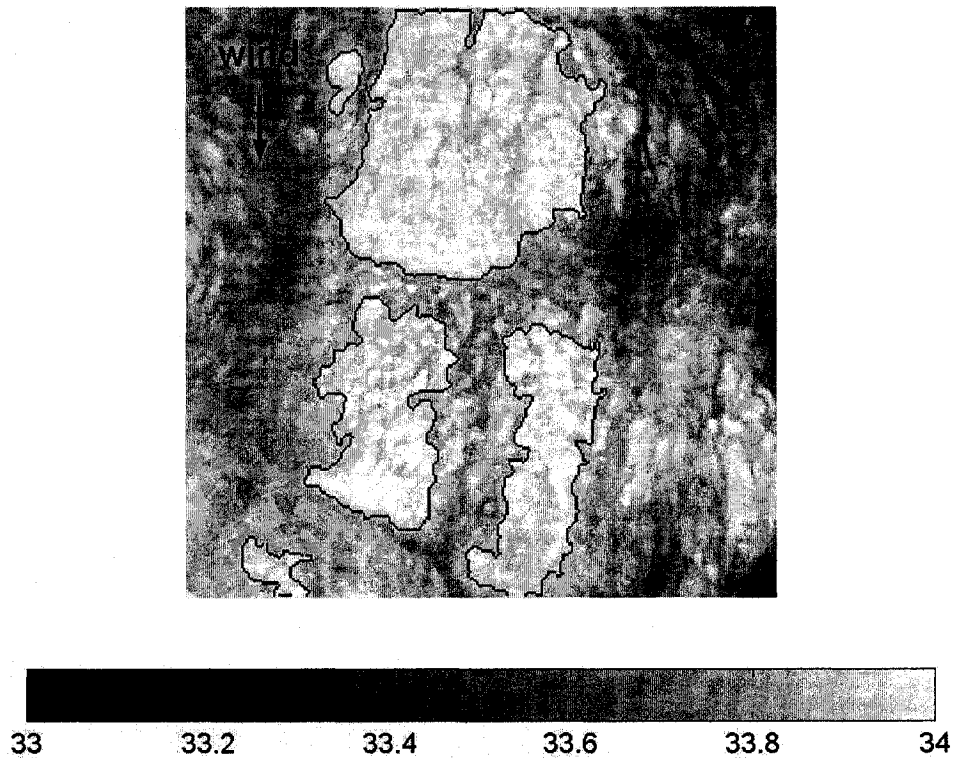


**Figure 1.3** An IR image at a wind speed of  $8.5 \text{ m s}^{-1}$ . The wake signatures produced due to the disruption of the cool skin layer by microscale breaking waves, are outlined in black. The dimensions of the IR image are  $34.3 \text{ cm} \times 34.3 \text{ cm}$  (Siddiqui, 2002)

Zappa (1999) and Zappa *et al.* (2001) examined the influence of microscale breaking waves on air-water gas and heat transfer using simultaneous infrared and wave slope imaging techniques. They found that the fraction of the area occupied by the thermal signatures of the turbulent wakes generated by microscale breaking waves was correlated with the gas and heat transfer velocities. They observed that the disruption of the skin layer coincides with waves that have a dimpled bore-like crest and steep forward face. More recently, Zappa *et al.* (2004) measured the local heat transfer velocities inside and outside these wakes generated by microscale breaking waves. They found that on average the heat transfer rate was enhanced by a factor of 3.5 inside the wakes and that microscale wave breaking directly contributed up to 75% of the transfer across the air-water interface under moderate wind speeds. Based on that, they concluded that microscale wave breaking is the underlying physical mechanism that determines the gas transfer rate at low to moderate wind speeds.

Siddiqui *et al.* (2001) presented preliminary results from a laboratory investigation of the flow fields beneath microscale breaking waves using simultaneously sampled and collocated IR imagery and Digital Particle Image Velocimetry (DPIV). They found that the wakes generated by microscale breaking waves were typically produced by a series of near-surface vortices that form behind the leading edge of the breaker. Strong correlations were observed between the near-surface vorticity and the local heat transfer velocity. The main conclusion was that the wakes produced by microscale breaking waves were regions of high near-surface vorticity that were in turn responsible for enhancing air-water heat transfer rates.

Peirson & Banner (2003) investigated the flow beneath microscale breaking waves using high-resolution DPIV measurements. Microscale breaking waves were detected using a scheme based on the local wave slope. They observed high values of the vorticity and surface convergence at the leading edge (or toe) of the breaking wave. They also argued that it is the subduction of the fluid at the toe that is responsible for the majority of the gas transfer.

In order to investigate the influence of the near-surface coherent structures, Siddiqui *et al.* (2004) computed the properties of these structures and developed a new parameterization of air-water gas transfer model using the coherent structure properties. They found that these coherent structures enhance the air-water gas transfer velocity by a factor of 2.8 and are responsible for 60% of the total air-water gas flux. The results also shown that in the regions occupied by coherent structures, turbulent kinetic energy was increased by a factor of 2.5.

Siddiqui and Loewen (2007) investigated the near-surface flows at a fetch of 5.5 m and wind speeds form 4.5 to 11  $\text{ms}^{-1}$  using simultaneous DPIV and infrared imagery. The results showed that in the crest-trough region beneath microscale breaking waves, 40% to 50% of the dissipation was associated with microscale wave breaking, which supports the premise that microscale breaking waves play a significant role in enhancing the transfer of gas and heat across the air-sea interface. These results also demonstrated that the enhanced near-surface turbulence in the wind drift layer was the result of microscale wave breaking. Their results also validated the proposal by Terray *et al.* (1996) which stated that the rate of dissipation of turbulent kinetic energy due to wave breaking is a function of depth, friction velocity, wave height and phase speed.

### **1.1.1.2 Surface Contamination**

Surfactants or surface-active agents are described as molecular species located at the surface of a liquid (Jones and Toba 2001). They are comprised of a hydrophobic (water-fearing) part and a hydrophilic (water-loving) part, so that they can obtain an equilibrium state at an interface between aqueous and non-aqueous phases (e.g. air-sea interface). Mass & Milgram (1998) have shown that most natural sea surfactant molecules have sufficient surface tension to form surface films over a wide range of ocean surfaces. They also mentioned that the main surfactant sources in the open sea are phytoplankton exudates and the chemical breakdown of dead organisms.

Zappa (1999) conducted a laboratory study to investigate the effect of microscale breaking waves on air-water gas transfer for clean and surfactant-contaminated water surfaces using IR and wave slope imagery. He found that the surfactants reduced the gas transfer velocity and damped the capillary waves.

Ceniceros (2003) numerically studied the effects of surfactants on the formation and evolution of small capillary ripples on the forward face of short waves. A hybrid methodology was used in this study to couple the full two-phase Navier-Stokes equations with a free boundary and the effect of surfactant. He found that surfactants affected capillary waves dramatically and the capillary region was regularly marked by an accumulation of surfactant concentration. He also concluded that the size of wave roller, the amplitude and the wavelength were reduced by surfactants.

Surfactants not only affected the wave field through wave damping but also modified the surface boundary conditions. In the absence of wind, the only surface stress acting at a clean air-water interface (i.e. free of surfactants) is surface tension. Lang & Gharib

(2000) found that surfactants typically reduce the surface tension in proportion to their concentration at the free surface. Therefore, when surfactant concentration varies along a free surface, surface tension gradients are produced. They also showed that the generation of surface tension gradients results in the production of shear stresses which alters the surface boundary conditions. Finally, they concluded that surfactants are important to the dynamics of free surface flows because of their influence on the behavior of near-surface turbulence.

Jokardris (2004) reported on a laboratory investigation of the near-surface flow beneath clean and contaminated wind-driven water surfaces using simultaneous infrared imagery and DPIV. Her results showed that surfactants reduced the energy of dominant waves by approximately 40% to 60%. The mean velocity profiles confirmed the existence of a viscous sublayer where the mean velocity varies linearly with depth. She also showed that within the viscous sublayer, the mean streamwise velocity gradients were two or three times larger beneath the surfactant-contaminated surfaces than that of the clean surfaces, which generated a thin layer of enhanced vorticity beneath the surfactant-contaminated surfaces. The results also demonstrated that surfactants did not affect the amplitude and length of capillary waves. However, they reduced the number of capillary waves by 50-70% and the number of gravity waves with parasitic capillary waves by 30-60%. She concluded that surfactants reduced the percentage of breaking by approximately 50% due to the damping of the capillary waves.

Kamash (2005) conducted an experimental study on the effect of surfactants on microscale wave breaking and the aqueous boundary layer using DPIV. He found that at all speeds (3.8 to 9.8m.s<sup>-1</sup>) the flow in the aqueous boundary layer was in the transition



regime for both water surface conditions (clean and contaminated). He also observed a strong negative correlation between the fraction of the total momentum transferred to the aqueous boundary layer and the mean square wave slope irrespective of the water surface condition. The ratio of the dissipation rate of turbulent kinetic energy in contaminated water to that in clean water decreased from 1.0 to 0.7 as the wind speed increased from 3.8 to 9.8m.s<sup>-1</sup>. Surfactants reduced the enhanced layer of near-surface turbulence on average by 35%. The surfactants reduced the percentage of wave breaking by approximately one third and reduced the wave amplitude and maximum wave slope on the forward face of the waves by an average factor of 25% and 28%, respectively for breaking waves and 22% and 19%, respectively for non-breaking waves. He also explained that irrespective of the water surface condition, there is a strong correlation between the fraction of the total momentum transferred to the wave field and the percentage of breaking waves.

### **1.1.2 Numerical Studies on Water Waves**

As mentioned earlier, the numerical investigation of water waves is difficult due to its three-dimensional nature and flow interactions between air and water. Furthermore, the location of free surfaces which changes with time and space is usually unknown and its determination is one of the major challenges faced by numerical investigations. In the numerical modeling of free surface flows, the following approaches are used: pure Lagrangian method, Eulerian method, and arbitrary Lagrangian Eulerian method (ALE). In the Lagrangian method, the equations of the fluid particles whose location changes continuously with time need to be employed. There are two distinguished advantages of

Lagrangian method; one is that there is no convective acceleration term in the Lagrangian formulations and the problem is immediately self-adjoint, the second is that it is possible for the free surface to be updated and maintained during the fluid motion. However, this method is not commonly used in fluid mechanics due to large deformations in fluids in comparison to solids.

The computational methods used to describe the evolution of the interface can be distinguished into two broad classes, namely: interface tracking methods and interface capturing methods (see Figure 1.4). Interface tracking methods (Ferziger and Perić 1999) are used in a Lagrangian fashion to evolve the interface, for example, by evolving marker particles (Figure 1.4a) or by adapting meshes with the interface profiles (Figure 1.4b). The notable characteristic and advantage of the interface tracking methods is that the exact location of the interface is known. Other advantages include simple and accurate incorporation of surface tension calculations and the precise imposition of boundary conditions. However, there are also two disadvantages of such a method. One is that it is usually more complex to implement than capturing methods. The other is that this kind of method is not suitable when interfaces are likely to merge and rupture.

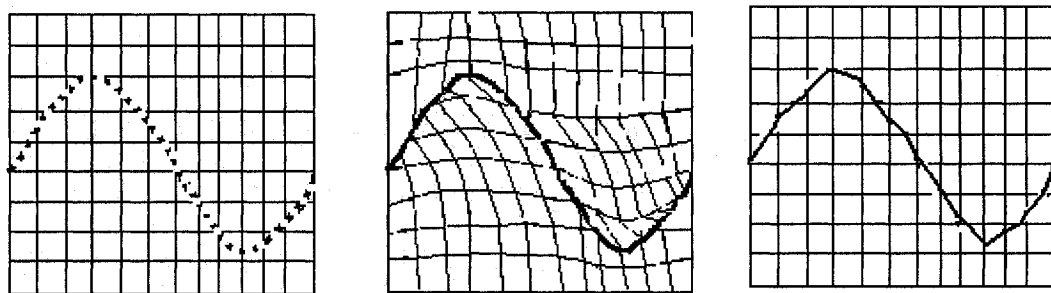


**Figure 1.4:** Methods of representing an interface (a) marker particles; (b) an adaptive mesh; (c) volume tracking.

Gotoh and Sakai (1999) performed a Lagrangian numerical simulation of breaking waves using the Moving Particle Semi-implicit (MPS) method. In this study, the breaking waves were simulated on several bottom configurations, namely uniform slope, permeable uniform slope and vertical wall with small step on its foot. The authors drew the conclusion that the particle method, including MPS method can be used to simulate the wave breaking process. The advantage of the particle method is that it is the free form of numerical diffusion due to the advection terms in the Navier-Stokes equation, which is a common disadvantage in the Eulerian method. However, the particle method takes much longer CPU time and also needs much more memory than that for the Eulerian method.

Dalrymple & Rogers (2006) presented a new model, called Smoothed Particle Hydrodynamics (SPH) to simulate free surface flows. SPH is a mesh-free Lagrangian method. The equivalent of mesh points are the fluid particles moving with the flow. One notable advantage of this method is that it does not require any special approaches to trace the surface, such as the volume-of- fluid method or a Lagrangian surface tracking. Furthermore, this method can also deal with rotational flows with vorticity and turbulence. They have shown that their method could model breaking waves on beaches in two and three dimensions, green water overtopping of decks, and wave-structure interaction. This method, however, is not suitable to model large areas because it does require a large number of particles in the simulation for resolution.

In the Eulerian method, the boundaries of the fluid motion and computational meshes are fixed in position. For free surface flows, the problem arises immediately as the locations of the interface, or free surface is unknown. Therefore, an additional algorithm,

namely the interface capturing (volume) method needs to be incorporated to trace the free surface. This is carried out by solving a convection equation for the free surface height on the free boundary. The main advantage of the Eulerian method is that it can be used to solve problems where the free boundaries undergo large deformations that Lagrangian methods cannot handle. The major disadvantage is the numerical diffusion due to the existence of the advection terms in the Navier-Stokes equations, especially when there is a free surface boundary.

Volume tracking is the most common method of an interface capturing technique. In this method, the location of the interface on a fixed mesh is replaced by some indications of fluid volume (see Figure 1.4c). It was developed from the concept of Marker-and-Cell (MAC) proposed by Harlow and Welch (1965). Volume tracking assigns a scalar function to each cell to indicate the fraction of the cell volume filled with the fluid. Volume tracking techniques can be classified into two categories according to the way the scalar values are used to reconstruct and advect the interface. The first refers to the older methods characterized by an interface reconstruction that aligns fluid with the fixed mesh. The second one is the more recent PLIC (Piecewise Linear Interface Calculation) method, which defines the surface in terms of linear (or planar, in three dimensions) interfaces within each cell (Rider and Kothe 1998).

Hirt and Nichols (1981) presented the Volume of Fluid (VOF) method, which is now considered to be the most famous volume tracking method. They considered Eulerian formulations for problems involving free boundaries. VOF method was compared with other free boundary methods, such as height functions, line segments and marker particles, in terms of their discrete representation, their evolution in time, and the manner in which

boundary conditions were imposed on them. The results showed that VOF method was more flexible and efficient than other methods for treating complicated free boundary flows. The VOF method has been incorporated into a number of well known algorithms such as, SOLA-VOF (Nichols and Hirt 1975) and RIPPLE (Kothe, Mjolsness and Torrey 1991).

Chen and Kharif (1999) conducted numerical simulations of plunging breakers using Direct Numerical Simulations (DNS). The numerical modeling of this two-phase flow is based on a piecewise linear version of VOF method. A stress tensor calculated from the gradients of the volume fraction function was considered to account for capillary or surface tension effects. Results showed concurrence with the laboratory observations of breaking water wave motions including overturning, plunging process, air entrainment and successful splash-up cycles. The generation of vorticity both in the liquid and gas was also observed during the breaking process. It was also found that the energy dissipation due to viscosity played a significant role in the formation of splash-up.

Since both the Lagrangian and Eulerian methods have advantages and disadvantages, a new method called arbitrary Lagrangian Eulerian method (ALE) provides another alternative to secure the best features of both Lagrangian and Eulerian descriptions by combining them.

Nithiarasu (2005) presented an arbitrary Lagrangian Eulerian (ALE) method for non-breaking free surface flow problems. The Characteristic-Based Split (CBS) scheme was used to solve the ALE equations. The author also mentioned that the major difference of this method from other existing finite element based methods was the way in which the mesh velocity was calculated. A simple mesh smoothing algorithm, which was based on

determining the position of the node by simple averaging the coordination of the surrounding nodes, was used in the calculations. Such a smoothing was applied during each time interval. Finally it was concluded that results showed agreement with available experimental data.

## **1.2 Motivations**

Waves can be generated and propagated in various fluids or media, such as sound and water. Of all the various types of fluid wave motion that occur in nature, surface water waves are not only the most commonly observed but are also of great practical importance because of their impact on coastal and offshore structures and ship dynamics. Also, their implications for sediment transport and coastal morphology and their overall effect on the energy and momentum exchange between the atmosphere and oceans are important. Previous studies have shown that microscale breaking waves play a very important role in controlling the flux of heat, gas and momentum across the air-water interface.

The flow field beneath wind waves is complex due to the presence of three components of velocity namely mean, wave and turbulent, and their interactions. The experimental investigations in the near-surface region beneath wind waves are challenging due to the fluctuation of the water surface and the complexity of the turbulent flow in this region. The numerical investigations are also difficult due to the three-dimensional nature of the flow and flow interactions. Although there have been some experimental studies conducted on flow beneath microscale breaking waves, few of these

numerical investigations have been done in this field, especially in three-dimensional simulations of small scale wind-driven water wave.

Most of nature's seas are contaminated on the surface. It has been demonstrated that most surfactant molecules that have drifted onto the surface of natural seas have sufficient surface tension to form surface films over a wide range of ocean surfaces. Previous studies have shown that contaminated surfactant films have a significant effect on the gas, heat, and energy exchange between air and sea.

Therefore, this study will focus on a numerical analysis of near surface flow beneath clean and contaminated small-scale wind-driven water waves. Also, some three-dimensional simulations will be run to give us a qualitative impression on three-dimensional wind-driven water waves.

### **1.3 Objectives**

Previous studies already demonstrated that microscale wave breaking plays a significant role in the process of gas and heat transfer between air and water. Some experimental investigations in the near-surface region beneath wind waves have been done by researchers to better understand the structure, the average properties and the importance beneath microscale breaking waves. However, little research has been done on numerical simulation of such microscale breaking wave due to the three-dimensional nature of the flow and flow interactions.

The specific objectives of this thesis are to:

- 1) Numerically investigated the effect of wind speed on the properties of near surface flow beneath small-scale wind driven water waves. The properties include the mean

streamwise velocity distribution as a function of depth, the dominated wavelength and the RMS amplitude.

- 2) Numerically analyze the effect of surface contamination on average properties beneath small-scale wind waves, including the mean streamwise velocities, the mean amplitude and the dominated wavelength.
- 3) Qualitatively analyze the three-dimensional effect on the generation and propagation of small-scale wind-driven water waves.

## **1.4 Thesis Organization**

An introduction, motivation and objective of the thesis and relative literature review are presented in Chapter I. In Chapter II, the methodologies used in the research, including numerical techniques that have been used in this study and a simple description of the experimental setup are explained in detail. Chapter III is about model validation. In this chapter, the mesh size independence of the model is first presented and then the numerical results are validated by the experimental data. All of the numerical simulation results are presented and discussed in Chapter IV. Finally, in Chapter V, conclusions of the thesis are summarized and some future work in this area is recommended.



# Chapter II

## Methodology

### 2.1 Numerical Studies

The small scale wind generated water waves are modeled as a transient three-dimensional incompressible fluid flow. A Volume of Fluid (VOF) method, provided by Youngs (1982, 1992), is used to track the transient air-water interface. The surface tension or the free surface energy is also taken into account due to its significant effect at these scales. It is modeled as a continuous, three-dimensional force across the interface using Continuum Surface Force (CSF) model (Brackbill *et al.* 1992). The Finite Difference method is used to solve the governing equations based on an Eulerian, rectilinear mesh in Cartesian and a two-step projection method is used to solve the time discretization momentum equation.

When the surface of the ocean is contaminated, a surface-active film is generated at the interface. This surface-active film tends to lower the free surface energy, and thus lower the surface tension. Therefore, the effect of surface contaminations is modeled by changing the surface tension force across the air-water interface.

#### 2.1.1 Governing Equations

The process of small-scale wind-generated water waves can generally be considered as a viscous, incompressible and Newtonian free surface fluid flow. Governing equations used to describe this process include equations of mass and momentum

conservation. In the present study, the variation of temperature is assumed to be negligible, thus be decoupled from the velocity and pressure field. Therefore, the continuity (equation 2.1) and the momentum (equation 2.2) equations can be stated as:

$$\nabla \cdot \vec{V} = 0 \quad (2.1)$$

$$\frac{\partial \vec{V}}{\partial t} + \nabla \cdot (\vec{V} \vec{V}) = -\frac{1}{\rho} \nabla p + \frac{1}{\rho} \nabla \cdot \vec{\tau} + \vec{g} + \frac{1}{\rho} \vec{F}_b \quad (2.2)$$

where  $\rho$ ,  $\vec{V}$ ,  $p$  are the fluid density, velocity, and pressure, respectively. Also  $\vec{\tau}$  represents the viscous stress tensor.  $\vec{g}$  is the acceleration due to gravity, and  $\vec{F}_b$  is the body force other than gravitational force.

In equation 2.2,  $\vec{\tau}$  is the viscous stress tensor. Since the fluid is Newtonian,

$$\vec{\tau} = \mu (\nabla \vec{V} + (\nabla \vec{V})^T) \quad (2.3)$$

where  $\mu$  represents the liquid dynamic viscosity.

Meanwhile, an additional equation is required to capture the air-water interface. At the surface, a fixed Eulerian frame with the VOF technique is used to reconstruct free surfaces. It is implemented by introducing a scalar field  $f(\vec{x}, t)$ , where

$$f(\vec{x}, t) = \begin{cases} 1 & \text{in the liquid} \\ > 0, < 1 & \text{at the free surface} \\ 0 & \text{in the void} \end{cases} \quad (2.4)$$

Here,  $f$  is a Lagrangian scalar function and is advected at the end of each computational cycle after completing the second step of the projection method according to the following equation,

$$\frac{df}{dt} = \frac{\partial f}{\partial t} + (\vec{V} \cdot \nabla) f = 0 \quad (2.5)$$

### 2.1.2 Volume of Fluid (VOF) Method

A brief introduction about volume tracking methods is provided in Chapter 1. All the volume tracking methods consist of two parts; an approximate of the interface reconstruction and an evaluation of fluid flux across cell faces (the volume fraction advection). Maintaining a very sharp interface (limited to one or two cells) is very important for a volume tracking method in order to guarantee the numerical stability. There has been several volume advection techniques developed for finite volume or finite difference methods aimed at maintaining a sharp interface. Among these, the most famous ones are SLIC (the Simplified Line Interface Calculation) method reported by Noh and Woodward (1976), the Volume of Fluid (VOF) method introduced by Hirt and Nichols (1981) and finally, Youngs method (1982).

The algorithm implemented in this model is that of Youngs. Youngs' method was initially developed as a 2D algorithm (Youngs 1982), and then later extended to 3D (Youngs 1992). This algorithm used a Piecewise Linear Interface Calculation (PLIC) to reconstruct the interface, which is considered to be a more accurate interface reconstruction than either Hirt-Nichols' VOF or SLIC.

In Youngs' scheme, the interface is reconstructed by locating a plane within each interface cell according to the volume fraction  $f_{i,j,k}$  and the normal of the interface,  $\hat{n}_{i,j,k}$ . An estimate is first made of the interface orientation,  $\hat{n}_{i,j,k}$ . The interface within a cell is then approximated by a straight line segment with the estimated orientation, which cuts the cell in such a way that the fractional fluid volume is given by  $f_{i,j,k}$ . In 2D, the interface is a line crossing the cell and in 3D the line extends to a three- to six-sided polygon,

depending on how the plane intersects the cell. As it is shown in Figure 2.1b, it is not necessary for the adjacent interface planes to be continuous in the interface reconstruction.

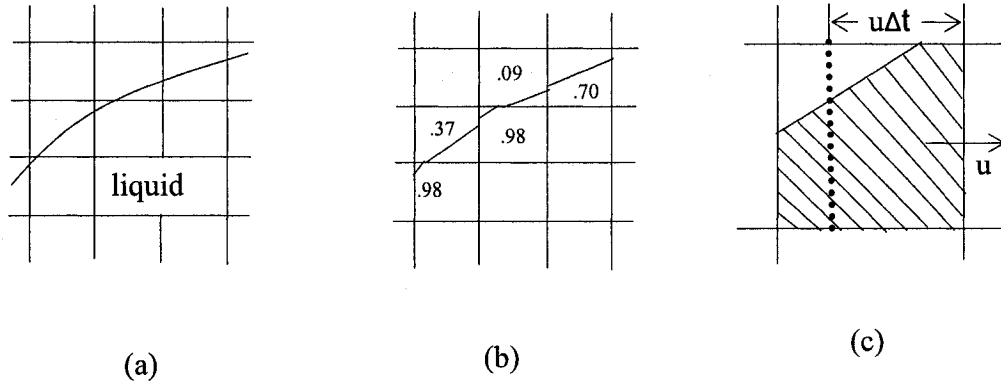


**Figure 2.1:** Volume fraction advection in 2D: (a) an exact liquid interface; (b) corresponding  $f_{i,j,k}$  and the associated planar interface; (c) with  $u$  positive, the shaded region to the right of the dashed line is advected into the neighboring cell.

During each timestep, the fluxes of the fluid across the interface are determined by the location of the interface and the velocities at the cell faces. Figure 2.1c is a simple illustration of 2D volume advection. In 3D, a specific technique entitled “Operator Split” provided by Rider and Kothe (1998) is used to minimize the directional bias. In this algorithm, the volume fluxes are calculated only one dimension at a time, which is followed by an interim interface reconstruction. By alternating the advection order from one timestep to the next, the directional bias is considered to be minimized.

### 2.1.3 The Two-Step Projection Method

The finite difference method is used to discretize the momentum equation (Equation 2.2) in the computational domain. A time discretization of the momentum equation (Equation 2.2) is given by

$$\frac{\bar{V}^{n+1} - \bar{V}^n}{\delta t} = -\nabla \cdot (\bar{V}\bar{V})^n - \frac{1}{\rho^n} \nabla p^{n+1} + \frac{1}{\rho^n} \nabla \cdot \tau^n + \bar{g}^n + \frac{1}{\rho^n} \bar{F}_b^n \quad (2.6)$$

where  $p$  is the scalar pressure field of the flow. It can be easily seen that the only implicit term in Equation 2.6 taken at the advanced time  $t^{n+1}$  is the pressure term. All of the other terms including advection, viscosity, gravity, and body forces are estimated by their values at the old time  $t^n$ .

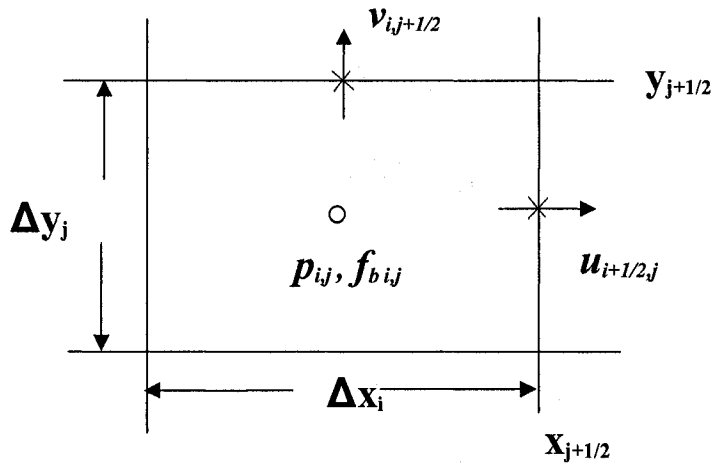


**Figure 2.2:** A 2D view of cell  $(i,j,k)$ . Velocities  $u,v,w$  (normal to the page-not shown) are specified at the centre of cell faces, pressure  $p$  and body force  $F_b$  at the cell centre.

The two-step projection method is the basic algorithm used to solve the governing equations for the incompressible flow. The idea of this algorithm is to break up Equation 2.5 which is a time discretization of Equation 2.2, into two steps. The two steps are shown as follows:

$$\text{Step 1: } \frac{\tilde{\bar{V}} - \bar{V}^n}{\delta t} = -\nabla \cdot (\tilde{\bar{V}}\bar{V})^n + \frac{1}{\rho^n} \nabla \cdot \tau^n + \bar{g}^n + \frac{1}{\rho^n} \bar{F}_b^n \quad (2.7)$$

$$\text{Step 2: } \frac{\bar{V}^{n+1} - \tilde{\bar{V}}}{\delta t} = -\frac{1}{\rho^n} \nabla p^{n+1} \quad (2.8)$$

In the first step,  $\tilde{\vec{V}}$  is a velocity field calculated from the incremental changes of  $\vec{V}^n$  resulting from viscosity, advection, gravity and body forces. In the second step, this velocity field is projected onto a zero-divergence vector field (i.e.  $\nabla \cdot \vec{V}^{n+1} = 0$ ). The combination of the two equations in the second step generates the following single Poisson equation for the pressure, known as the “Pressure Poisson Equation” (PPE).

$$\nabla \cdot \left[ \frac{1}{\rho^n} \nabla p^{n+1} \right] = \frac{\nabla \cdot \tilde{\vec{V}}}{\delta t} \quad (2.9)$$

Note that the density  $\rho$  on the right hand side of Equation 2.7 is the density of the incompressible liquid. However, in Equation 2.9, the density is retained inside the divergence operator, which is used to smooth the pressure distribution within the free surface transition region.

In summary, given velocity, pressure, and volume fraction fields at time  $n$ , the solution at time  $n+1$  can be obtained by the following algorithm:

- 1) Evaluate  $\tilde{\vec{V}}$  via Equation 2.7
- 2) Solve the Poisson Equation 2.9 to obtain the value  $p^{n+1}$
- 3) Evaluate  $\vec{V}^{n+1}$  via Equation 2.8 and apply boundary conditions on  $\vec{V}^{n+1}$
- 4) Update the fluid volume fraction distribution  $f^{n+1}$  using Equation 2.5
- 5) Reapply boundary conditions on  $\vec{V}^{n+1}$

#### 2.1.4 Momentum Convection

Equation 2.7 is discretized using the finite volume method. The integration of Equation 2.7 over a control volume  $\Omega_{i,j,k}$  yields:

$$\frac{1}{\Delta t} \int_{\Omega_{i,j,k}} (\tilde{\vec{V}} - \vec{V}^n) d\Omega = - \int_{\Omega_{i,j,k}} \nabla \cdot (\vec{V} \vec{V})^n d\Omega + \frac{1}{\rho} \int_{\Omega_{i,j,k}} \nabla \cdot \vec{\tau}^n d\Omega + \int_{\Omega_{i,j,k}} \vec{g}^n d\Omega + \frac{1}{\rho} \int_{\Omega_{i,j,k}} \vec{F}_b^n d\Omega \quad (2.10)$$

Applying Gauss' theorem over the control volume surface  $S_{i,j,k}$  to the above equation and assuming the integrands are constant throughout  $\Omega_{i,j,k}$  (except the first two volume integrals on the right hand side), Equation 2.10 becomes:

$$\frac{\tilde{\vec{V}} - \vec{V}^n}{\Delta t} = - \frac{1}{\Omega_{i,j,k}} \int_{S_{i,j,k}} \vec{V}^n (\vec{V}^n \cdot \hat{n}_s) dS + \frac{1}{\rho \Omega_{i,j,k}} \int_{S_{i,j,k}} (\vec{\tau}^n \cdot \hat{n}_s) dS + \vec{g}^n + \frac{1}{\rho} \vec{F}_b^n \quad (2.11)$$

where  $\hat{n}_s$  is the unit outward normal to  $S_{i,j,k}$  and the first term of Equation 2.11 is called the convective term.

Figure 2.3 illustrates the x-component of the convective term of Equation 2.11 applied to the shaded control volume about the velocity  $u_{i+1/2,j,k}$ .

$$\begin{aligned} - \frac{1}{\Omega_{i,j,k}} \int_{S_{i,j,k}} u (\vec{V}^n \cdot \hat{n}_s) dS = & - \frac{u_{i+1,j,k}^f \langle u \rangle_{i+1,j,k} - u_{i,j,k}^f \langle u \rangle_{i,j,k}}{\Delta x_{i+\frac{1}{2}}} - \frac{v_{i+\frac{1}{2},j+\frac{1}{2},k}^f \langle u \rangle_{i+\frac{1}{2},j+\frac{1}{2},k} - v_{i+\frac{1}{2},j-\frac{1}{2},k}^f \langle u \rangle_{i+\frac{1}{2},j-\frac{1}{2},k}}{\Delta y_i} \\ & - \frac{w_{i+\frac{1}{2},j,k+\frac{1}{2}}^f \langle u \rangle_{i+\frac{1}{2},j,k+\frac{1}{2}} - w_{i+\frac{1}{2},j,k-\frac{1}{2}}^f \langle u \rangle_{i+\frac{1}{2},j,k-\frac{1}{2}}}{\Delta z_k} \end{aligned} \quad (2.12)$$

In the above equation,  $u^f$ ,  $v^f$ , and  $w^f$  represent the transport rates of the quantity  $\langle u \rangle$  in and out of the control volume in the x, y and z direction respectively, as illustrated in Figure 2.3. The definition of  $\Delta x_{i+\frac{1}{2}}$  is as following,

$$\Delta x_{i+\frac{1}{2}} = \frac{\Delta x_i + \Delta x_{i+1}}{2} \quad (2.13)$$

$\Delta y_{j+\frac{1}{2}}$  and  $\Delta z_{k+\frac{1}{2}}$  have the similar expression. The x and y components of the momentum convective term can be written correspondingly.

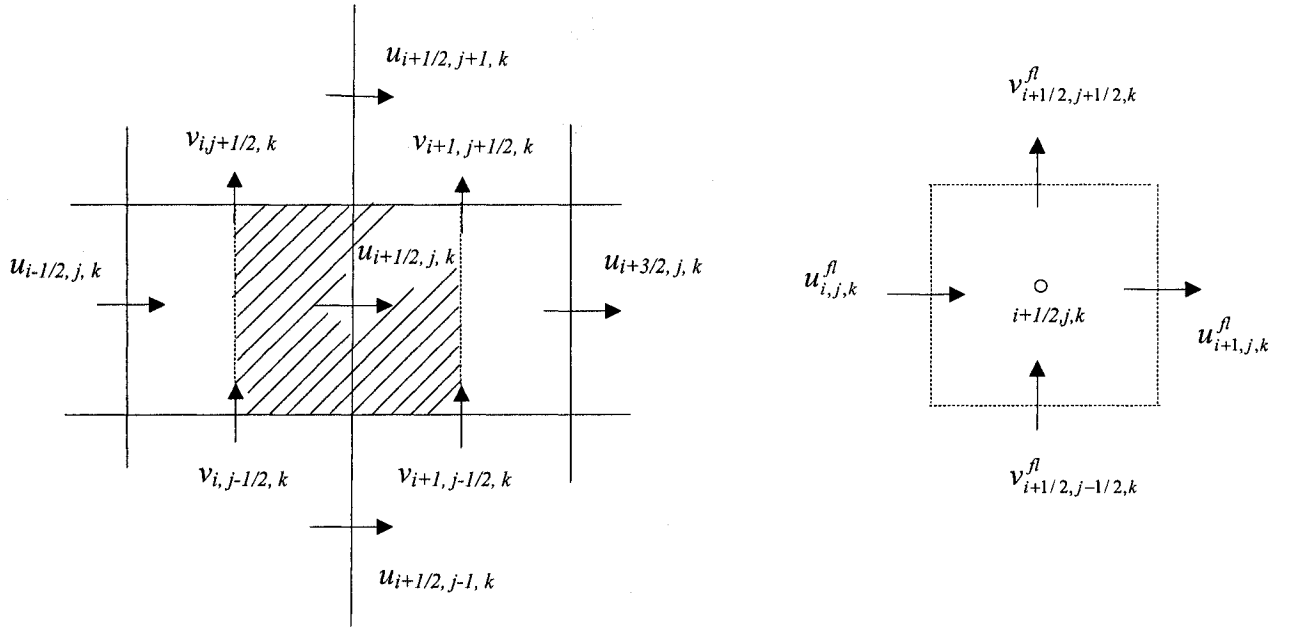


**Figure 2.3:** (a) the x-component momentum control volume about the velocity  $u_{i+\frac{1}{2},j,k}$ ; (b) the interpolated flux velocities at the control volume faces.

The flux velocities are calculated by the interpolation of neighboring velocities:

$$u_{i,j,k}^{fl} = \frac{u_{i-\frac{1}{2},j,k} + u_{i+\frac{1}{2},j,k}}{2}$$

$$u_{i+1,j,k}^{fl} = \frac{u_{i+\frac{1}{2},j,k} + u_{i+\frac{3}{2},j,k}}{2}$$



$$\begin{aligned}
v_{i+\frac{1}{2},j-\frac{1}{2},k}^f &= \frac{\Delta x_{i+1} v_{i,j-\frac{1}{2},k} + \Delta x_i v_{i+1,j-\frac{1}{2},k}}{\Delta x_i + \Delta x_{i+1}} \\
v_{i+\frac{1}{2},j+\frac{1}{2},k}^f &= \frac{\Delta x_{i+1} v_{i,j+\frac{1}{2},k} + \Delta x_i v_{i+1,j+\frac{1}{2},k}}{\Delta x_i + \Delta x_{i+1}} \\
w_{i+\frac{1}{2},j,k-\frac{1}{2}}^f &= \frac{\Delta x_{i+1} v_{i,j,k-\frac{1}{2}} + \Delta x_i v_{i+1,j,k-\frac{1}{2}}}{\Delta x_i + \Delta x_{i+1}} \\
w_{i+\frac{1}{2},j,k+\frac{1}{2}}^f &= \frac{\Delta x_{i+1} v_{i,j,k+\frac{1}{2}} + \Delta x_i v_{i+1,j,k+\frac{1}{2}}}{\Delta x_i + \Delta x_{i+1}}
\end{aligned} \tag{2.14}$$

Using van Leer's method (van Leer 1979), the estimates for the flux quantities  $\langle u \rangle$  in x direction between two cells filled with liquid are given by:

$$\langle u \rangle_{i,j,k} = \begin{cases} u_{i-\frac{1}{2},j,k} + \frac{\Delta x}{2} \alpha^{vL} \left( \frac{\partial u}{\partial x} \right)_{i-\frac{1}{2},j,k} \left[ 1 - \frac{u_{i,j,k}^f \Delta t}{\Delta x_i} \right] & u_{i,j,k}^f > 0 \\ u_{i+\frac{1}{2},j,k} + \frac{\Delta x}{2} \alpha^{vL} \left( \frac{\partial u}{\partial x} \right)_{i+\frac{1}{2},j,k} \left[ 1 + \frac{u_{i,j,k}^f \Delta t}{\Delta x_i} \right] & u_{i,j,k}^f < 0 \end{cases} \tag{2.15}$$

where the velocity gradients are approximated as:

$$\begin{aligned}
\left( \frac{\partial u}{\partial x} \right)_{i-\frac{1}{2},j,k} &= \frac{u_{i+\frac{1}{2},j,k} - u_{i-\frac{3}{2},j,k}}{\Delta x_{i-1} + \Delta x_i} \\
\left( \frac{\partial u}{\partial x} \right)_{i+\frac{1}{2},j,k} &= \frac{u_{i+\frac{3}{2},j,k} - u_{i-\frac{1}{2},j,k}}{\Delta x_i + \Delta x_{i+1}}
\end{aligned} \tag{2.16}$$

In Equation 2.15, the quantities in square brackets change the Taylor expansion to the center of the flux center. The flux quantities  $\langle u \rangle$  in the y and z directions can be estimated similarly.

In the van Leer method,  $\alpha^{vL}$  is a coefficient satisfying  $0 \leq \alpha^{vL} \leq 1$  and is used to guarantee the numerical stability by introducing enough upwinding to the central difference approximation. When  $\alpha^{vL} = 0$ , Equation 2.15 is actually a first order upwind approximation, and when  $\alpha^{vL} = 1$ , this equation is a conditionally unstable second order central difference approximation. The introduction of  $\alpha^{vL}$  can also ensure locally monotonic velocity distributions from one time step to the next one. The flux quantities  $\langle u \rangle$  in the y and z directions can be estimated similarly. The van Leer limiter  $\alpha^{vL}$  is estimated by:

$$\alpha^{vL} = \max[0, \min(\alpha_1, \alpha_2, 1)] \quad (2.17)$$

In the above equation,  $\alpha_1$  and  $\alpha_2$  are defined as:

$$\alpha_1 = \frac{u_{\max} - \min \left[ u_{i-\frac{1}{2},j,k}, u_{\max} \right]}{\max \left[ 0^+, u_{\max}^g - u_{i-\frac{1}{2},j,k} \right]} \quad (2.18)$$

$$\alpha_2 = \frac{\max \left[ u_{i-\frac{1}{2},j,k}, u_{\max} \right] - u_{\min}}{\max \left[ 0^+, u_{i-\frac{1}{2},j,k} - u_{\min}^g \right]} \quad (2.19)$$

where  $u_{\min}$  and  $u_{\max}$  are local minimum and maximum velocities and  $0^+$  represents a small positive value (e.g.  $10^{-6}$ ), chosen to avoid division by zero.

$$u_{\min} = \min \left[ u_{i+\frac{1}{2},j,k}, u_{i-\frac{3}{2},j,k} \right] \quad (2.20)$$

$$u_{\max} = \max \left[ u_{i+\frac{1}{2},j,k}, u_{i-\frac{3}{2},j,k} \right] \quad (2.21)$$

and  $u_{\min}^g, u_{\max}^g$  are minimum and maximum velocities respectively.

$$u_{\min}^g = \min[u_R^g, u_L^g] \quad (2.23)$$

$$u_{\max}^g = \max[u_R^g, u_L^g] \quad (2.24)$$

resulting from unlimited Taylor expansions:

$$u_R^g = u_{i-\frac{1}{2},j,k} + \frac{\Delta x_i}{2} \left( \frac{u_{i+\frac{1}{2},j,k} - u_{i-\frac{3}{2},j,k}}{\Delta x_{i-1} + \Delta x_i} \right) \quad (2.25)$$

$$u_L^g = u_{i-\frac{1}{2},j,k} - \frac{\Delta x_{i-1}}{2} \left( \frac{u_{i+\frac{1}{2},j,k} - u_{i-\frac{3}{2},j,k}}{\Delta x_{i-1} + \Delta x_i} \right) \quad (2.26)$$

The above van Leer's method can only be applied to estimate flux quantities between two cells filled with liquid. Since the velocities outside of liquid phase are undefined, it is difficult to apply to the control volume containing part of the interface. Strict upwind differencing (corresponding to  $\alpha^{VL} = 0$ ) is used to estimate flux quantities when the control volume contains part of the interface.

## 2.1.5 Viscosity

As mentioned before, the liquid is assumed to be Newtonian. Therefore, the shear stress tensor  $\vec{\tau}$  can be defined as:

$$\vec{\tau} = \mu (\nabla \vec{V} + (\nabla \vec{V})^T) \quad (2.26)$$

where  $\mu$  is the liquid dynamic viscosity. Expanding the viscous term in momentum Equation 2.2, results in equation 2.2.8:

$$\nabla \cdot \vec{\tau} = \left( \frac{\partial \tau_{xx}}{\partial x} + \frac{\partial \tau_{yx}}{\partial y} + \frac{\partial \tau_{zx}}{\partial z} \right) \hat{i} + \left( \frac{\partial \tau_{xy}}{\partial x} + \frac{\partial \tau_{yy}}{\partial y} + \frac{\partial \tau_{zy}}{\partial z} \right) \hat{j} + \left( \frac{\partial \tau_{xz}}{\partial x} + \frac{\partial \tau_{yz}}{\partial y} + \frac{\partial \tau_{zz}}{\partial z} \right) \hat{k} \quad (2.27)$$

As an example, the discretization in the x direction is as followings (see Figure 2.4).

$$\left( \frac{\partial \tau_{xx}}{\partial x} + \frac{\partial \tau_{yx}}{\partial y} + \frac{\partial \tau_{zx}}{\partial z} \right) \bigg|_{i+\frac{1}{2},j,k} = \frac{\tau_{xx,i+1,j,k} - \tau_{xx,i,j,k}}{\Delta x_{i+\frac{1}{2}}} + \frac{\tau_{yx,i+\frac{1}{2},j+\frac{1}{2},k} - \tau_{yx,i+\frac{1}{2},j-\frac{1}{2},k}}{\Delta y_j} + \frac{\tau_{zx,i+\frac{1}{2},j,k+\frac{1}{2}} - \tau_{zx,i+\frac{1}{2},j,k-\frac{1}{2}}}{\Delta z_k} \quad (2.28)$$

In the above equation, each shear stress tensor is approximated by simple velocity differences, as given below:

$$\begin{aligned} \tau_{xx,i+1,j,k} &= 2\mu \frac{u_{i+\frac{3}{2},j,k} - u_{i+\frac{1}{2},j,k}}{\Delta x_{i+1}} \\ \tau_{xx,i,j,k} &= 2\mu \frac{u_{i+\frac{1}{2},j,k} - u_{i-\frac{1}{2},j,k}}{\Delta x_i} \\ \tau_{yx,i+\frac{1}{2},j+\frac{1}{2},k} &= \mu \left( \frac{u_{i+\frac{1}{2},j+1,k} - u_{i+\frac{1}{2},j,k}}{\Delta y_{j+\frac{1}{2}}} + \frac{v_{i+1,j+\frac{1}{2},k} - v_{i,j+\frac{1}{2},k}}{\Delta x_{i+\frac{1}{2}}} \right) \\ \tau_{yx,i+\frac{1}{2},j-\frac{1}{2},k} &= \mu \left( \frac{u_{i+\frac{1}{2},j,k} - u_{i+\frac{1}{2},j-1,k}}{\Delta y_{j-\frac{1}{2}}} + \frac{v_{i+1,j-\frac{1}{2},k} - v_{i,j-\frac{1}{2},k}}{\Delta x_{i+\frac{1}{2}}} \right) \\ \tau_{zx,i+\frac{1}{2},j,k+\frac{1}{2}} &= \mu \left( \frac{u_{i+\frac{1}{2},j,k+1} - u_{i+\frac{1}{2},j,k}}{\Delta z_{k+\frac{1}{2}}} + \frac{w_{i+1,j,k+\frac{1}{2}} - w_{i,j,k+\frac{1}{2}}}{\Delta x_{i+\frac{1}{2}}} \right) \\ \tau_{zx,i+\frac{1}{2},j,k-\frac{1}{2}} &= \mu \left( \frac{u_{i+\frac{1}{2},j,k} - u_{i+\frac{1}{2},j,k-1}}{\Delta z_{k-\frac{1}{2}}} + \frac{w_{i+1,j,k-\frac{1}{2}} - w_{i,j,k-\frac{1}{2}}}{\Delta x_{i+\frac{1}{2}}} \right) \end{aligned} \quad (2.29)$$

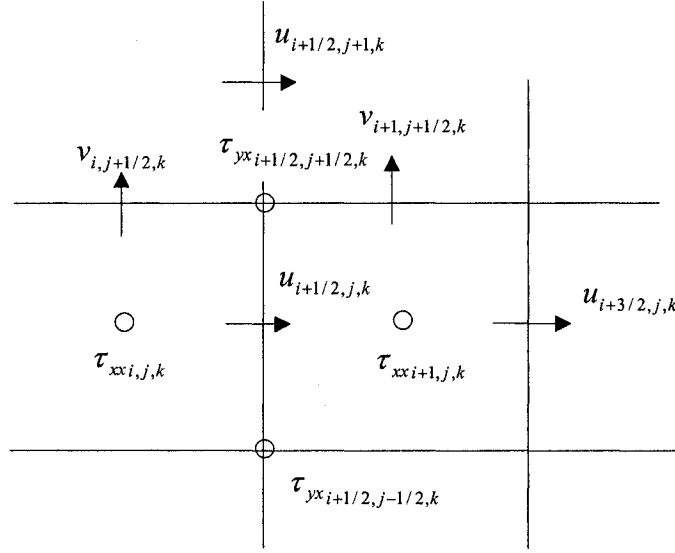


**Figure 2.4:** Shear stresses specified at the faces of an x-momentum control volume (note that the shear stresses related to z direction are not shown here)

Similarly, we can write the corresponding equations in the y and z directions.

### 2.1.6 The Gas Model and Other Boundary Conditions

To better incorporate the gas phase effect on the formation of wind-driven water waves, a gas model is implemented into the VOF solver to better estimate the wind velocity profile near the air-water interface. This gas model, which is given as the following dimensionless form, is based on the experimental data and the logarithmic law reported by Dattatri *et al.* (1977) .

$$u_* = 0.1271 * \log(U_{gas}) - 0.0162 \quad (2.30)$$

$$u = u_* \left( 5.75 \log \left( \frac{u_* y}{\nu_a} \right) + 5.0 \right) \quad (2.31)$$

where,  $u^*$ ,  $U_{gas}$ ,  $\nu_a$  and  $y$  represent the friction velocity, free stream gas velocity, kinematic viscosity of the air, and the distance from the interface, respectively. The gas velocity,  $u$ , varies with respect to the distance  $y$  and the free stream gas velocity. This gas model was validated by the experimental data conducted by Shaikh and Siddiqui 2007.

The boundary conditions for the numerical simulations are illustrated in Figure 2.5. A no slip boundary is applied at the bottom of the simulated tank. The periodic boundaries are imposed on left and right sides. The gas model described in this section above is applied as an open boundary at the air-water interface.

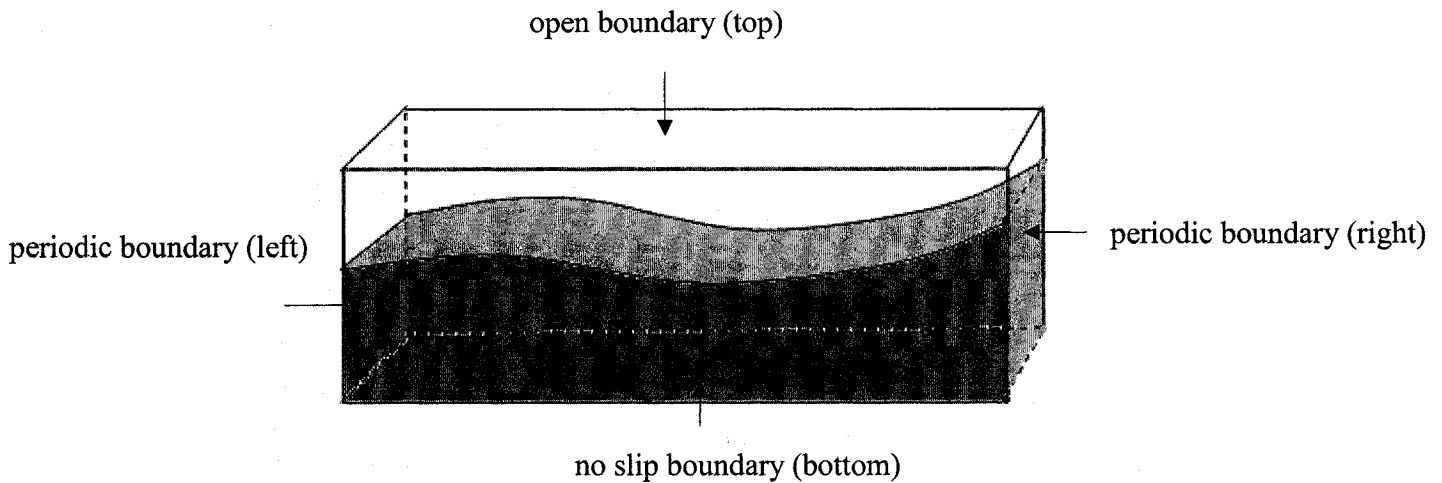


**Figure 2.5:** Scheme of boundary conditions for the simulated tank

For two-dimensional numerical simulation, we set the initial disturbance as a sine curve. The initial amplitude is 1.8mm, and the initial wavelength is 90mm for a wind speed of  $4.4\text{m}\cdot\text{s}^{-1}$ .

### 2.1.7 Timestep Restrictions

In order to guarantee the stability of the solution, the momentum and the fluid volume can only be advected into the neighboring cell, which implies that the Courant condition should be satisfied:

$$C = \max \left[ \frac{|u_{i,j,k}| \Delta t}{\Delta x_i}, \frac{|v_{i,j,k}| \Delta t}{\Delta y_j}, \frac{|w_{i,j,k}| \Delta t}{\Delta z_k} \right] < 1 \quad (2.32)$$

where  $\max[]$  is operated on cells for which  $f_{i,j,k} > 0$ . In practice, the Courant number is chosen less than 0.5. The results reported in this thesis were obtained with a Courant number set to 0.3. Similarly, momentum should be diffused with one cell per timestep.

$$\Delta t < \frac{\rho}{\mu} \cdot \min \left[ \frac{(\Delta x_i)^2 (\Delta y_j)^2}{(\Delta x_i)^2 + (\Delta y_j)^2}, \frac{(\Delta x_i)^2 (\Delta z_k)^2}{(\Delta x_i)^2 + (\Delta z_k)^2}, \frac{(\Delta z_k)^2 (\Delta y_j)^2}{(\Delta z_k)^2 + (\Delta y_j)^2} \right] \quad (2.33)$$

In order to better capture the characteristic of wind-driven water waves, the timestep should satisfy the following criterion,

$$\Delta t < \sqrt{\frac{\rho}{4\pi\gamma}} \cdot \min \left[ (\Delta x_i)^{1.5}, (\Delta y_j)^{1.5}, (\Delta z_k)^{1.5} \right] \quad (2.34)$$

Therefore, the chosen timestep at any time is the minimum value calculated by Equations 2.32, 2.33 and 2.34.

## 2.2 Experimental Study

### 2.2.1 Experimental Setup and Instrumentation

The experiments were conducted in a wind-wave flume shown as *Figure 2.6*. The flume is 3 m long and 0.9 m wide and 0.9 m high. The mean water depth was maintained at 0.45 m. At the downstream end of the tank, a horsehair beach is placed to absorb wave

energy. At the upstream end of the tank, a centrifugal fan was placed to produce wind speeds up to  $5\text{ m}\cdot\text{s}^{-1}$ . A schematic of the experimental setup and instrumentation is shown in Figure 2.7.

The two-dimensional velocity fields near the interface were measured using a Particle Image Velocimetry (PIV). The measurements were made in a plane parallel to the wind and bisecting the water surface at wind speeds of  $3.7\text{ m}\cdot\text{s}^{-1}$  and  $4.4\text{ m}\cdot\text{s}^{-1}$ . The PIV system consisted of a light source, camera, pulse generator and a PC equipped with a frame grabber. A Continuum Minilite 25 mJ Nd:YAG laser was used as a light source to illuminate the field of view of the PIV camera during the measurements. A four-channel digital delay generator (555-4C, Berkeley Nucleonics Corporation, San Rafael CA) was used to control the timing of the laser light pulses. The separation time between light pulses depends on the velocity range and the size of the interrogation region. That is, the accuracy of the PIV velocity estimates requires that the majority of the particles located in a given interrogation region in the first image to remain within the corresponding region search in the second image.

A CCD camera (JAI CV-M2) with the resolution of  $1600 \times 1200$  pixels was used to image the flow field. The field of view of the camera was set equal to 9 cm horizontal and 7 cm vertical. The vertical position of the camera was set in a way that the upper edge of the image was just a little bit higher (approximate 1.5 cm) than the position of the water surface. The camera was connected to a PC equipped with a frame grabber (DVR Express, IO Industries, London, ON, Canada) that acquired 8-bit images at a rate of 30 Hz. For each experimental run, the data was acquired for 5 minutes (i.e. 4500 images were acquired at a rate of 30 Hz).



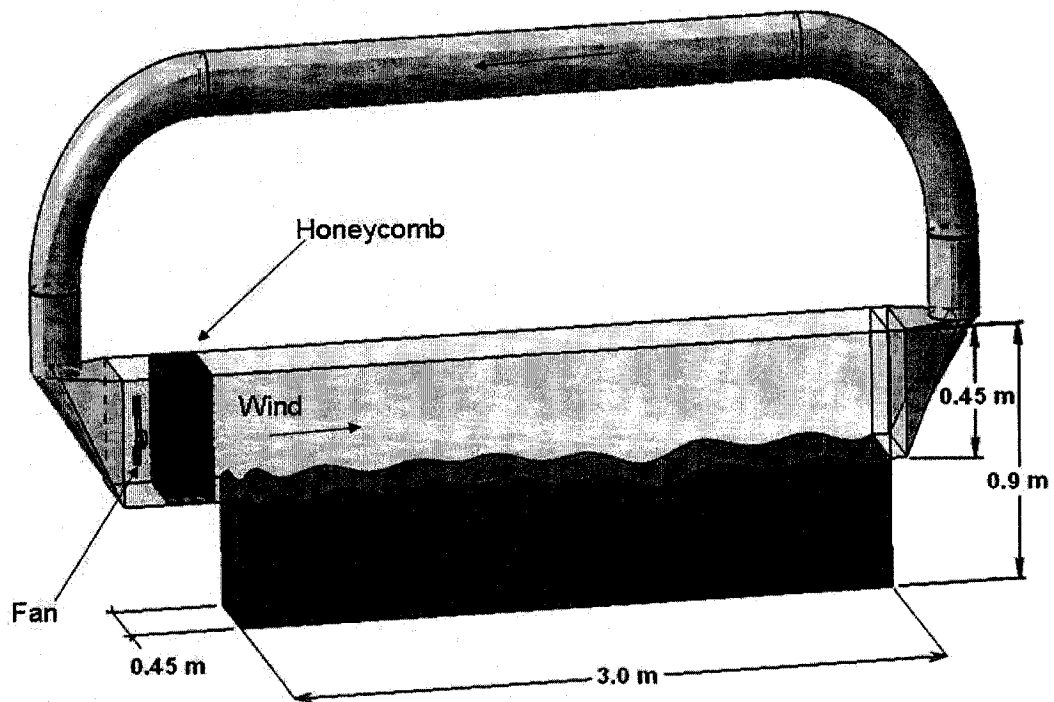


*Figure 2.6: Schematic of the experimental tank (Shaikh & Siddiqui, 2007)*

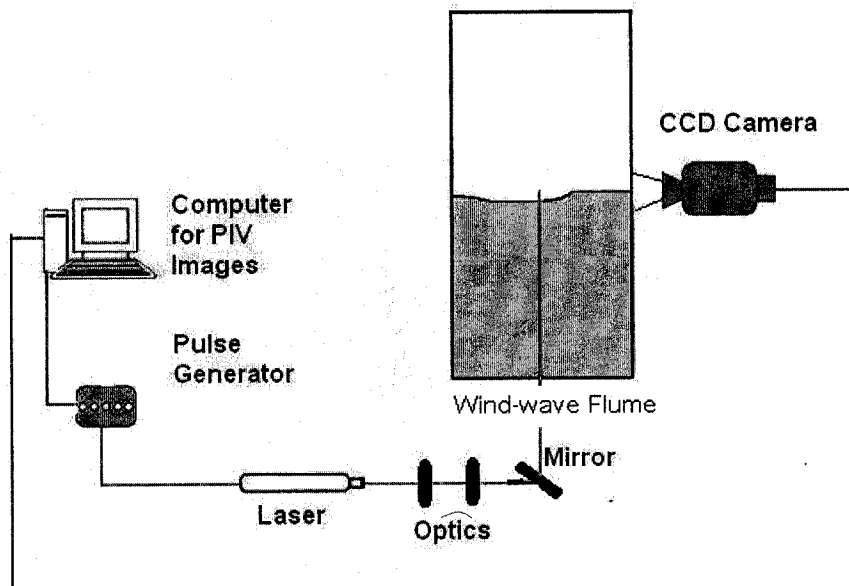


*Figure 2.7: Schematic of the experimental setup and instrumentation in the wind-wave flume (not to scale)*

### 2.2.2 PIV Technique

PIV is a relatively new optical imaging technique used to measure fluid or particulate velocity vectors at many (e.g. thousands) points in a flow field simultaneously. A typical PIV system (shown as in Figure 2.8) consists of a laser (used as a light source), optics used to generate a light sheet, CCD camera, pulse generator to control timing of the laser pulses and a PC equipped with a frame grabber. In this technique, the investigated fluid is seeded with tracer particles to follow the flow field. The test plane in the flow is first illuminated by a pulsed laser light sheet, and the positions of the particles of the test plane are recorded by the CCD camera at the same time. A short time later, the same test plane is illuminated by a second pulse and a second image of the particles is created by the camera. In this way, a series of image pairs are obtained. Figure 2.9 is the circuit diagram showing the timing of the laser pulse in the image pair. The timing and duration of each laser pulse is controlled by a pulse generator, which should be synchronized with the vertical sync signal sending from the CCD camera. In order to measure high velocity flow, the first laser pulse is usually set close to the end of the first frame and the second laser pulse after the beginning of the second frame.

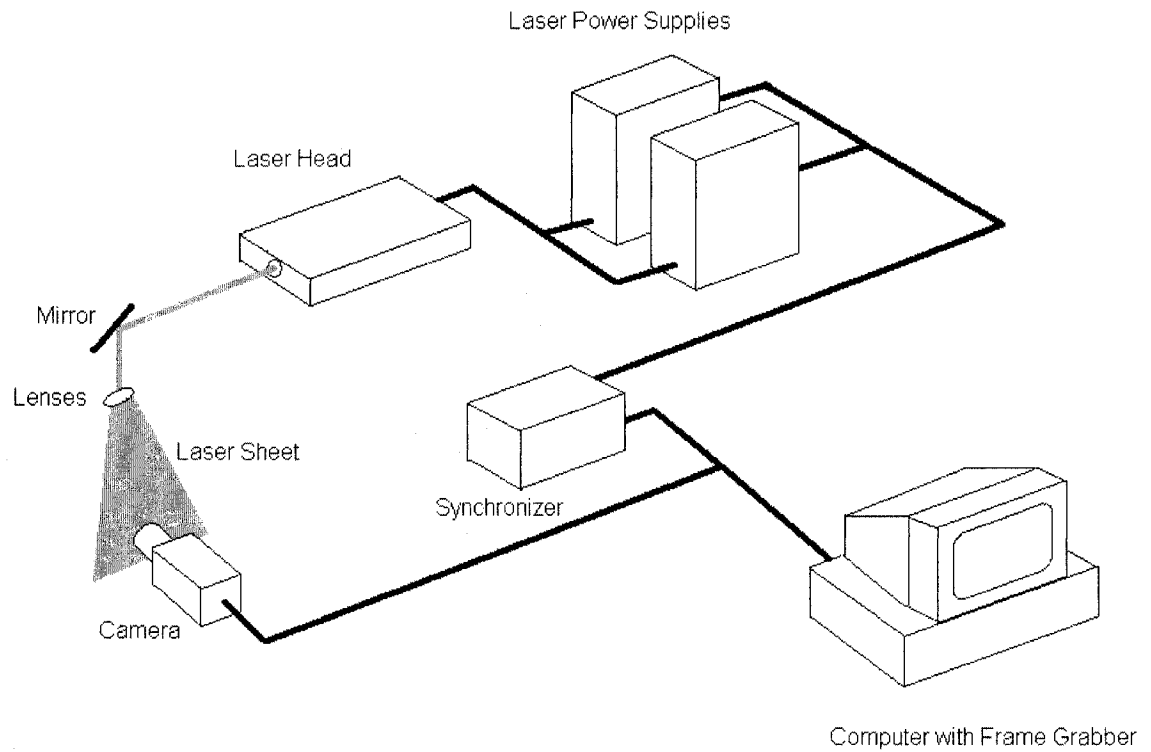


**Figure 2.8:** A schematics of a typical PIV system (Siddiqui 2002)

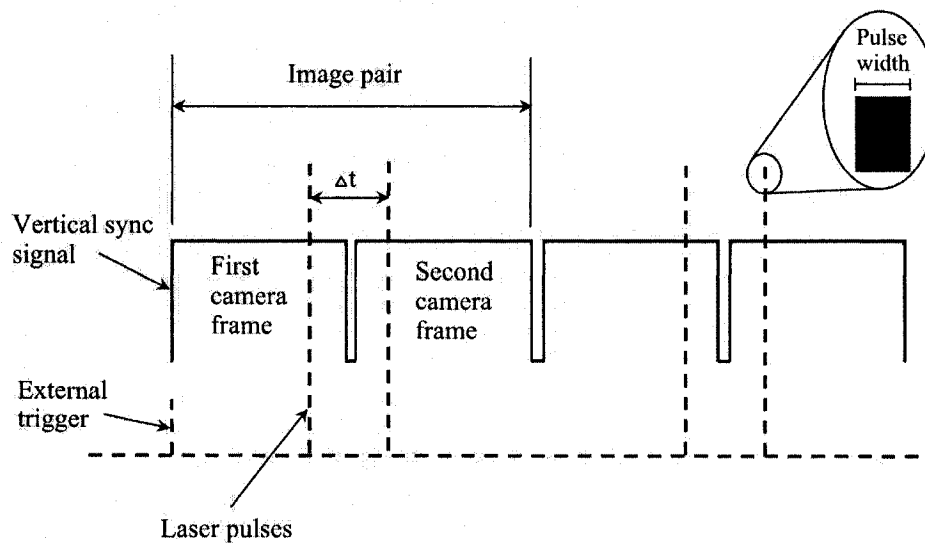


**Figure 2.9:** Circuit diagram showing the timing of the laser pulses in an image pair. A pulse generator controls the timing and duration of each laser pulse. (Siddiqui 2002)

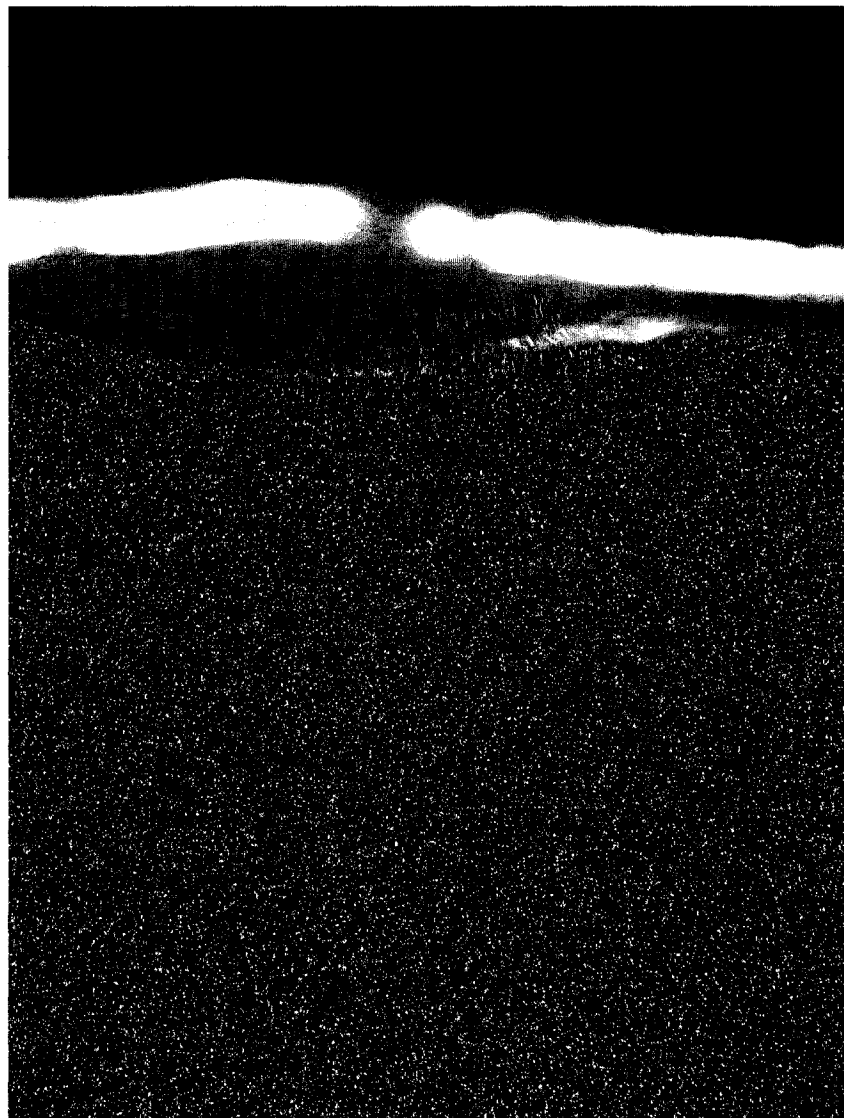
Seed particles were used to follow the flow field. But in most of the PIV images, these particles were reflected above the air-water interface, which may introduce errors in the computation of the velocity vectors for the interrogation window including part of the interface (Dabiri and Gharib 1997). A technique which is similar to the one presented by (Dabiri and Gharib 1997) was used in this study to minimize these errors by preprocessing the images. In this technique, the surface wave profile data were first used to locate the interface of the corresponding images. Then, the gray-scale values of all bright regions above a line that was two pixels below the measured water surface profile were set equal to the median gray-scale value of the image (i.e. equal to the background gray-scale value). The preprocessing interface was set two pixels below the actual interface in order to make sure that all reflections and false correlation peaks caused by reflection were eliminated.

When the preprocessing of all the PIV images was finished, the next step was to calculate the raw velocity fields using the algorithm written by Marxen (1998). Once the raw velocity vectors were obtained, the water surface profile data were used again to remove all the velocity vectors above the interface. The remaining velocity vectors were irregularly spaced and uncorrected (i.e. may contain spurious vectors). Siddiqui *et al.* (2001) developed a spurious vector scheme based on the local median test to detect the spurious vectors and replace them with the median of the neighboring velocity vectors. Typically, less than 1% of the velocity vectors were spurious. The corrected velocity vectors were then interpolated into a regular grid using an Adaptive Gaussian Window (AGW) interpolator (Agüí and Jiménez 1987).

### 2.2.3 Wave Profile Measurements

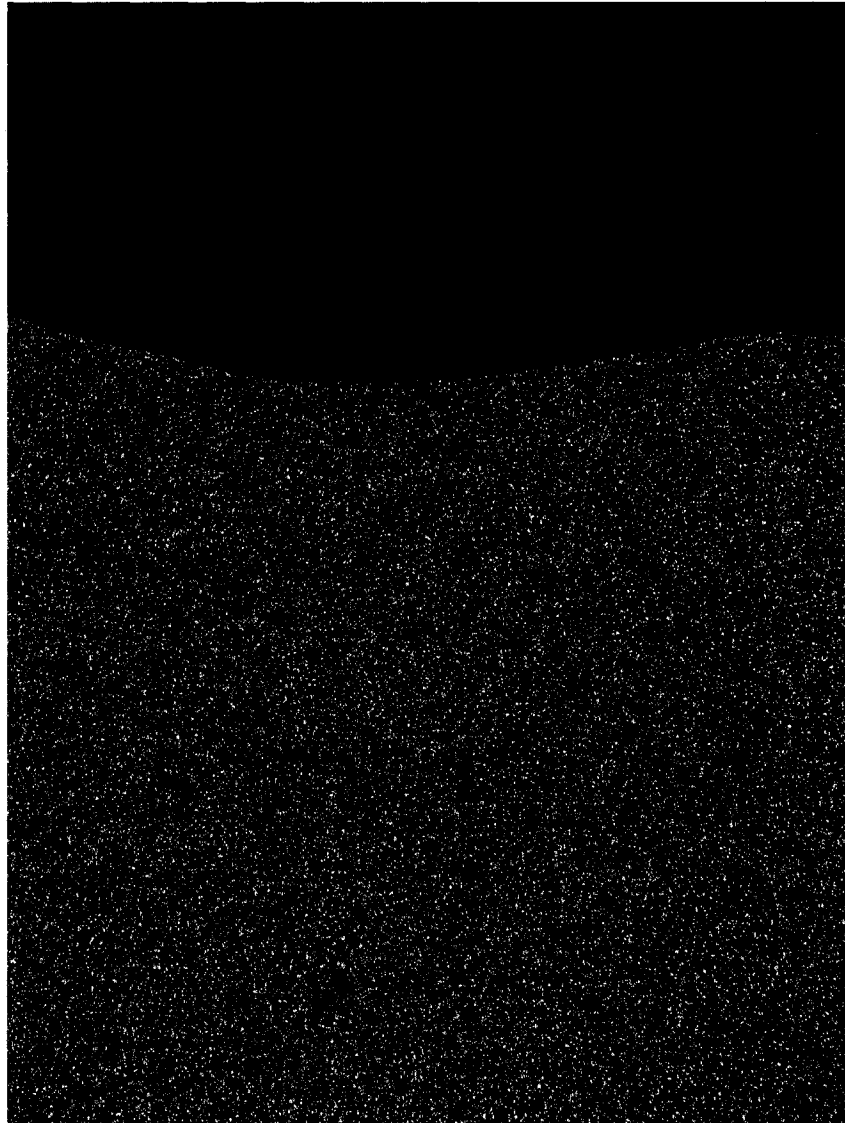
The typical original camera image was shown in Figure 2.10a. The first step with original images was to identify the water surfaces by hand and set the airside of the image as the background (see Figure 2.10b). Then an algorithm developed by Siddiqui *et al.* (2001) was used to record the locations of the water surfaces and marked as a white line (see Figure 2.10c).

→ Wind



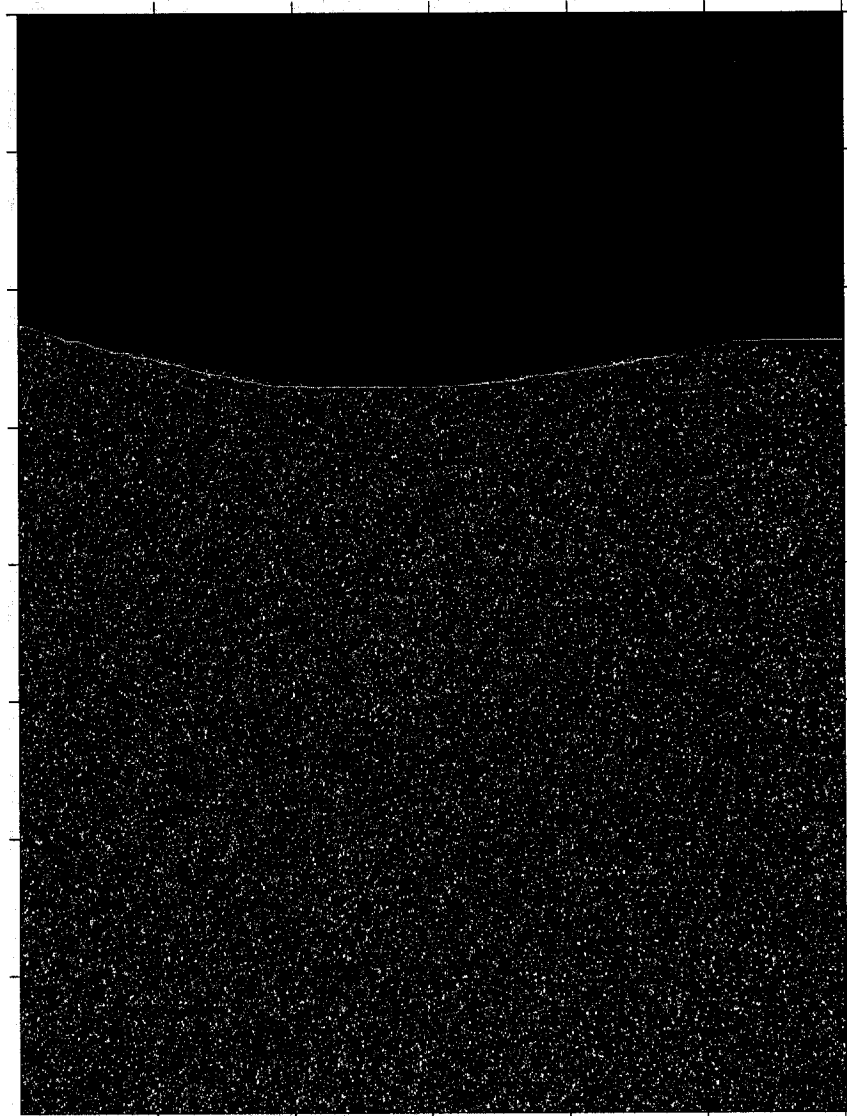
(a)

→ Wind



(b)

→ Wind



(c)

**Figure 2.10:** A typical PIV image at a wind speed of  $4.4 \text{ m. s}^{-1}$  (a) the original image; (b) after setting airside as background (c) computed surface wave profile plotted as a white line

## 2.2.4 Computation of the Instantaneous Velocity Fields

The procedures used to compute the instantaneous velocity fields from the PIV image pairs are described as followings:

1. Compute the surface wave profiles from the PIV images (as described in §2.3.3).
2. Import these surface wave profile data into the corresponding original PIV images.
3. Preprocess the PIV images and compute the raw velocity vectors using the cross-correlation algorithm (as described in §2.3.2).
4. Discard all the velocity vectors above the water surface.
5. Use the algorithm developed by Siddiqui *et al.* (2001) to detect and correct the spurious velocity vectors and then interpolate the new velocity vectors onto the regular grid (as described in §2.3.2).

This procedure is illustrated in Figures 2.9, 2.10, 2.11. A typical profile image at a wind speed of  $4.4 \text{ m.s}^{-1}$  with the measured surface wave profile overlaid on it, is shown in Figure 2.10. This surface wave profile data were then imported into the corresponding PIV image, shown in Figure 2.11. In Figure 1.11, bright regions and reflected particles can be clearly seen above the water surface. In order to remove false correlation peaks, all the bright pixels above the interface were set to the background gray-scale value. Figure 2.12 shows the velocity vectors after correction of the spurious vectors.



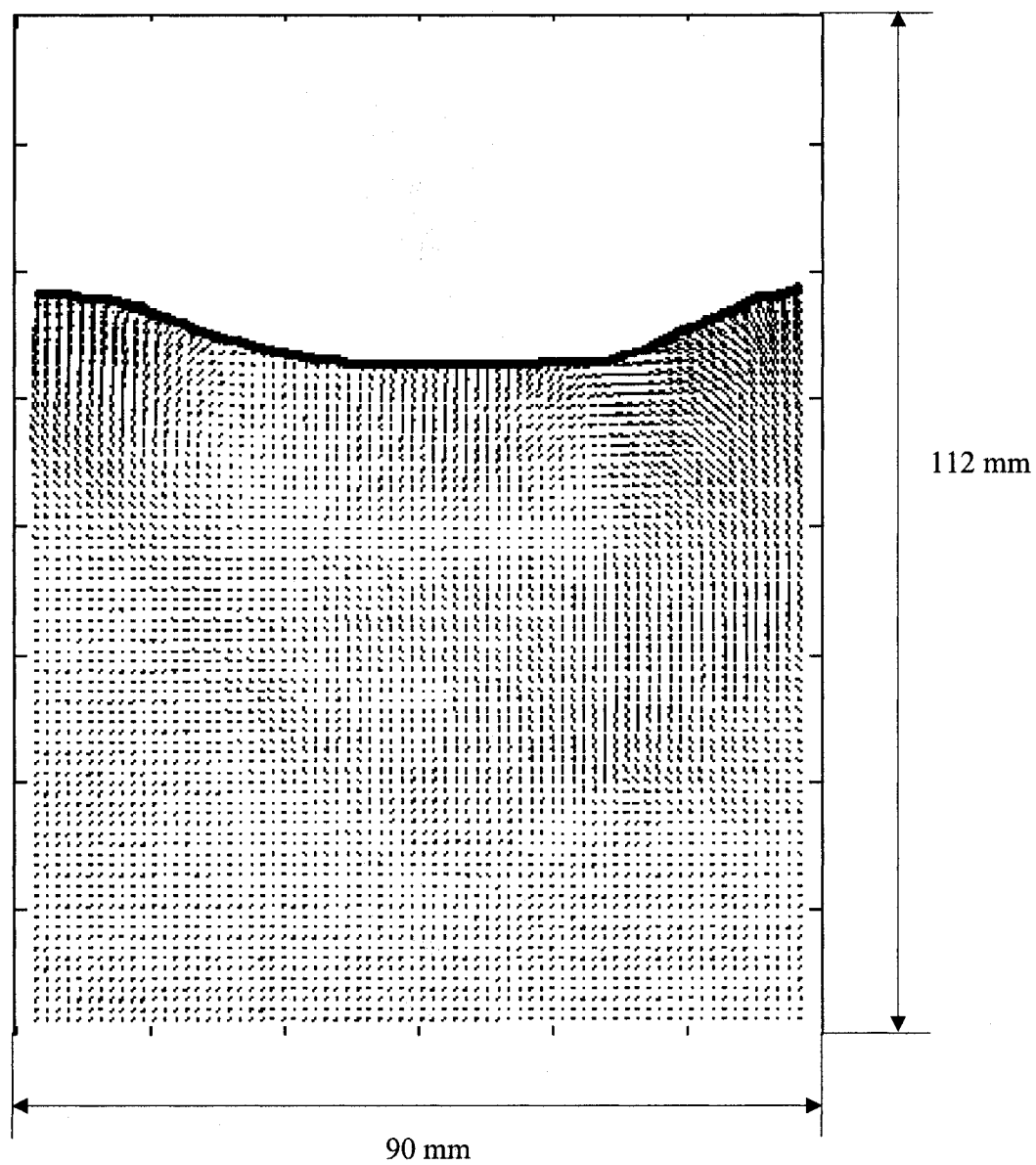


*Figure 2.11: The two-dimensional instantaneous velocity field obtained by processing the PIV image in Figure 2.10.*

### 2.2.5 Computation of Mean Velocity Components

Once the instantaneous velocity fields were computed from the PIV images (as described in §2.2.4), the procedure used to calculate the mean velocity components were as followings:

- 1) Transformed the corrected velocity vectors from a fixed Eulerian to a wave-following Eulerian system (Hsu *et al.* 1981). It means to develop a new coordinate system with the origin located at the air-water interface and rearrange the velocity vectors with reference to the free surface.
- 2) The mean velocity component was computed by time average the instantaneous velocity field in the new wave-following coordinate system.

The major factors that may result in errors in the PIV measurements include gradients, particle density, particle diameter, out-of-plane motion, dynamic range, peak locking and AGW interpolation (Cowen and Monismith 1997). The mean diameter of the seeded particles is 15  $\mu\text{m}$ . The largest error in the PIV measurements is expected to occur in the near surface region since the velocity gradient is the largest in this region. The errors were estimated in a 2 cm layer immediately below the water surface. Using the method described by Siddiqui in 2002, the maximum error in the velocity measurements was estimated to be 5%.

# Chapter III

## Model Validation

### 3.1 Gas Model Validation

As mentioned in Chapter 2, the gas model is developed and implemented into the VOF solver as the air-water interface. The gas model is validated by previous experimental data (Shaikh & Siddiqui 2007). Table 3.1 shows the comparisons of friction velocity,  $u_*$ , between experimental data and values estimated by the gas model according to equation 2.30. The table shows that the friction velocity calculated by the gas model concurs with the experimental data when the wind speed is no more than  $4.0\text{m}\cdot\text{s}^{-1}$ . The difference between the two is less than 6%. However, as the wind speed increases to  $4.4\text{m}\cdot\text{s}^{-1}$ , the friction velocity calculated by the gas model underestimates approximate 12% of the experimental datum.

**Table 3.1:** Friction velocity comparisons obtained from experimental data and the gas model (calculated by Equation 2.30)

Wind speed ( $\text{m}\cdot\text{s}^{-1}$ )	Experimental friction velocity ( $\text{cm}\cdot\text{s}^{-1}$ )	Friction velocity calculated by equation 2.30 ( $\text{cm}\cdot\text{s}^{-1}$ )
4.4	19.58	17.211
3.6	14.04	14.66
2.8	11.08	11.47
2.0	7.61	7.19

The wind velocity profile near the water surface obtained from the gas model and the experiment was presented in Table 3.2. As reported in Chapter 2,  $y$  in Equation 2.31 represents half of the grid size in the numerical simulations. A grid independent test has been performed to identify the required grid size (see appendix A). Therefore, a square grid with a size of 2mm is used throughout the studies. As a result, the estimated wind velocity required for the interface boundary condition is calculated at a height of 1mm above the water surface. The results show that the differences between the measured and estimated wind velocities are less than 10% for various wind speeds and heights above the interface. The maximum difference is located at a height of 2.67mm above the interface with a wind speed of  $3.6 \text{ m}\cdot\text{s}^{-1}$ . Using the method of interpolation, it can be deduced that the difference at a height of 1mm is approximately 5%. However, it can be also seen that the difference between the experimental data and estimated wind velocity obtained from the gas model increases with an increase in wind speed, which implies that the validity of proposed gas model is limited to the cases with wind speeds not more than  $5.0 \text{ m}\cdot\text{s}^{-1}$ .

**Table 3.2:** *Wind velocity distribution near the water surface obtained from experimental data and the gas model estimated by Equation 2.31*

Wind speed ( $\text{m}\cdot\text{s}^{-1}$ )	4.4			3.6		
Height away from the interface (mm)	0.53	1.6	2.67	0.53	1.6	2.67
Experimental data ( $\text{cm}\cdot\text{s}^{-1}$ )	139.88	183.97	217.26	120.1	169.68	201.95
Estimates by the gas model ( $\text{cm}\cdot\text{s}^{-1}$ )	147.46	194.67	216.63	127.87	162.64	181.6

### 3.2 Experimental Validation

The surface wave profile was recorded in both numerical and experimental studies. Typical surface wave profiles obtained from numerical simulations as well as experiments at a wind speed of  $4.4 \text{ m}\cdot\text{s}^{-1}$  are shown in Figures 3.1a and b, respectively. The dark portion in Figure 3.1b corresponds to the airside and bright portion showing the illuminated seed particles within the waterside. A white line is drawn to show the air-water interface. The numerical and experimental wave profiles show similar behavior. The similarities in the experimental and numerical wave profiles are quantified in terms of the wave characteristics computed from more than 2000 images from experimental runs and 300 frames obtained from the numerical simulation.

The wave properties that can be computed from the surface wave profile include the RMS wave height (mean amplitude), the dominant wave frequency ( $f_d$ ), and the dominant wavelength ( $\lambda_d$ ). Figure 3.2 shows frequency spectra computed from the experimental surface wave profile data at a wind speed of  $4.4 \text{ m}\cdot\text{s}^{-1}$ . The dominant frequency was the frequency corresponding to the maximum energy. Therefore, it can be seen from Figure 3.2 that the dominant frequency at a wind speed of  $4.4 \text{ m}\cdot\text{s}^{-1}$  is  $4.131 \text{ Hz}$ . The dominant wave length was calculated from the following deep-water dispersion relationship,

$$(2\pi f_d)^2 = g \left( 2 \frac{\pi}{\lambda_d} \right)$$

where,  $f_d$  is the dominant wave frequency,  $g$  is the acceleration due to gravity and  $\lambda_d$  is the dominant wavelength.

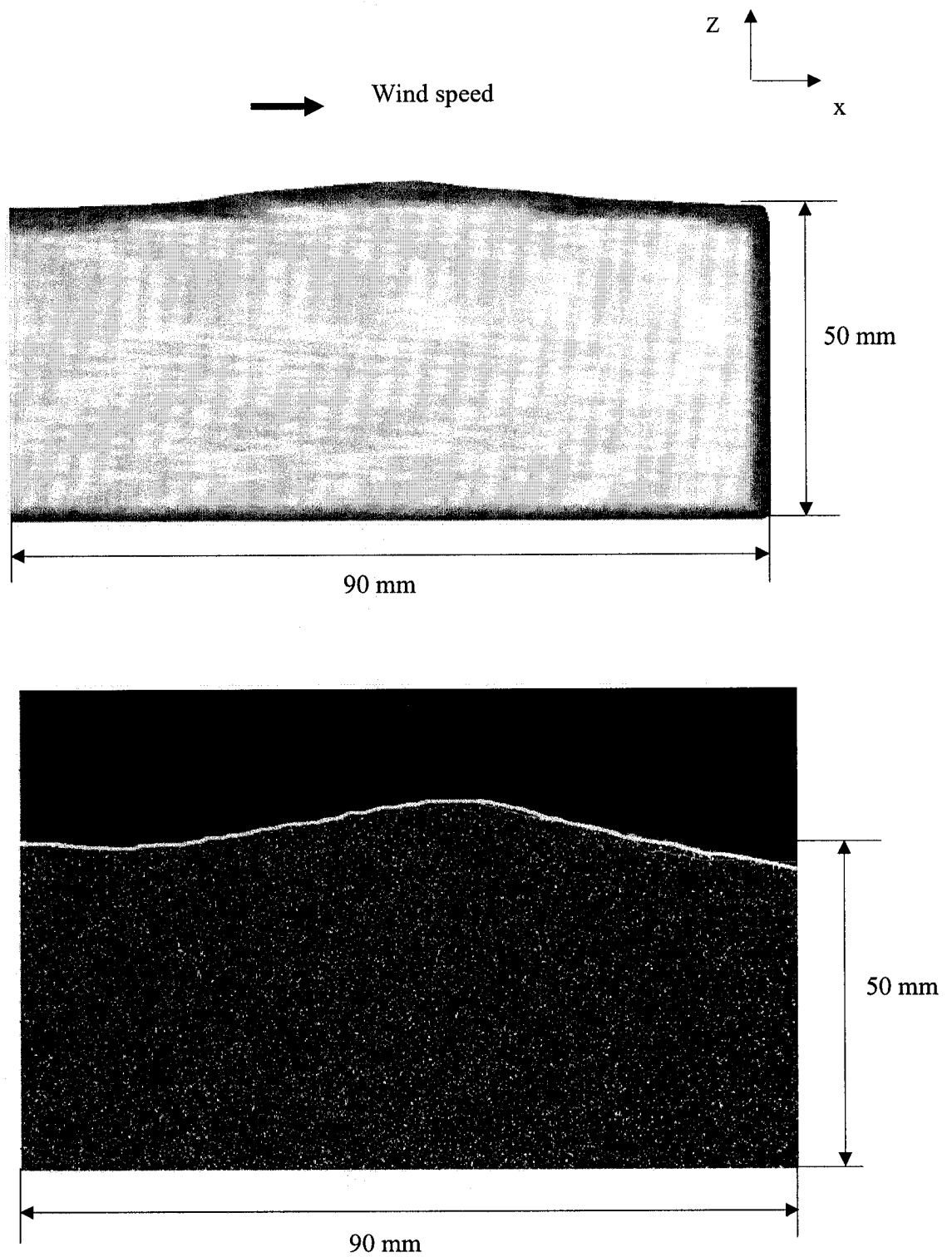


**Figure 3.1** A typical surface wave profile at a wind speed of  $4.4 \text{ m}\cdot\text{s}^{-1}$  obtained from (a) numerical simulation; (b) experimental data.

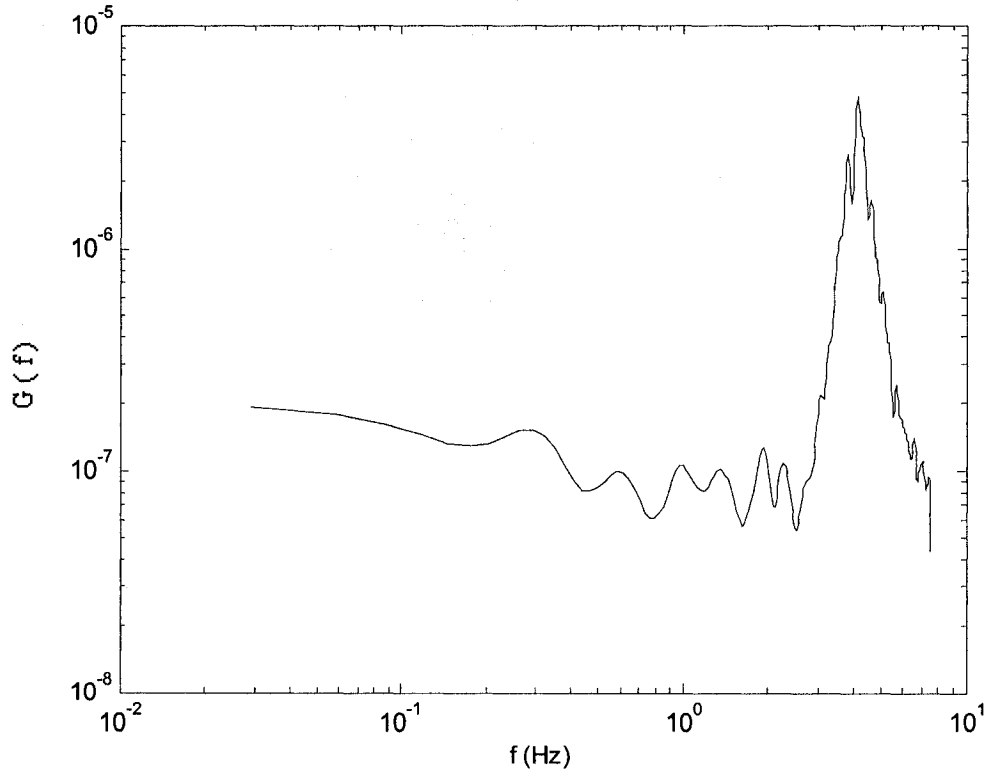


**Figure 3.2:** *Frequency spectra computed from experimental wave profile data at a wind speed of  $4.4 \text{ m}\cdot\text{s}^{-1}$ .*

The wave characteristics obtained from the numerical and experimental profiles are presented in Table 3.3. The difference between the RMS amplitude obtained from the numerical and experimental analyses at the wind speed of  $4.4 \text{ m}\cdot\text{s}^{-1}$  is  $0.2 \text{ mm}$  (i.e. about 10%). Moreover, for the dominant wavelength, the difference between the numerical and experimental studies is  $1.4 \text{ mm}$ . This difference is only 1.53% of the experimental datum. Therefore, a good agreement between the two can be identified, which confirms that the present numerical model is capable to simulate the free surface fluctuations and also implies that the gas model is appropriate when the wind speed is no more than  $4.4 \text{ m}\cdot\text{s}^{-1}$ .

**Table 3.3:** Wave characteristics obtained from numerical and experimental results

Wind speed ( $\text{m}\cdot\text{s}^{-1}$ )	RMS amplitude (mm)		Dominant wavelength (mm)	
	simulation	experiment	simulation	Experiment
4.4	1.8	2.0	90	91.4

The mean streamwise velocity profile at various depths and a wind speed of  $4.4 \text{ m}\cdot\text{s}^{-1}$  obtained from the numerical and experimental studies are plotted in Figure 3.3. Figure 3.3a illustrates the linear scale, while Figure 3.3b represents on the semi-logarithmic scale. The plots show excellent agreement between the numerical and experimental results at the interface and greater depths. In the region just below the water surface, the simulated velocities are slightly higher in magnitude than the experimental ones. The maximum difference between these two is  $0.2371 \text{ cm}\cdot\text{s}^{-1}$ , which is located at about 8 mm below the water surface. This difference is approximately 6.78% of the experimental result. The average difference of the mean streamwise velocities between the numerical and experimental results is approximately 2%. Considering the experimental uncertainties, the agreement between the experimental and numerical values is considered to be excellent. Siddiqui *et al.* (2004), Siddiqui & Loewen (2007) and Cheung *et al.* (1988) investigated the near surface flow of small scale wind waves and provided evidences for a logarithmic velocity distribution near small-scale wind driven water surface. In Figure 3.3b, both velocity profiles show logarithmic behavior, which is consistent with previous studies.



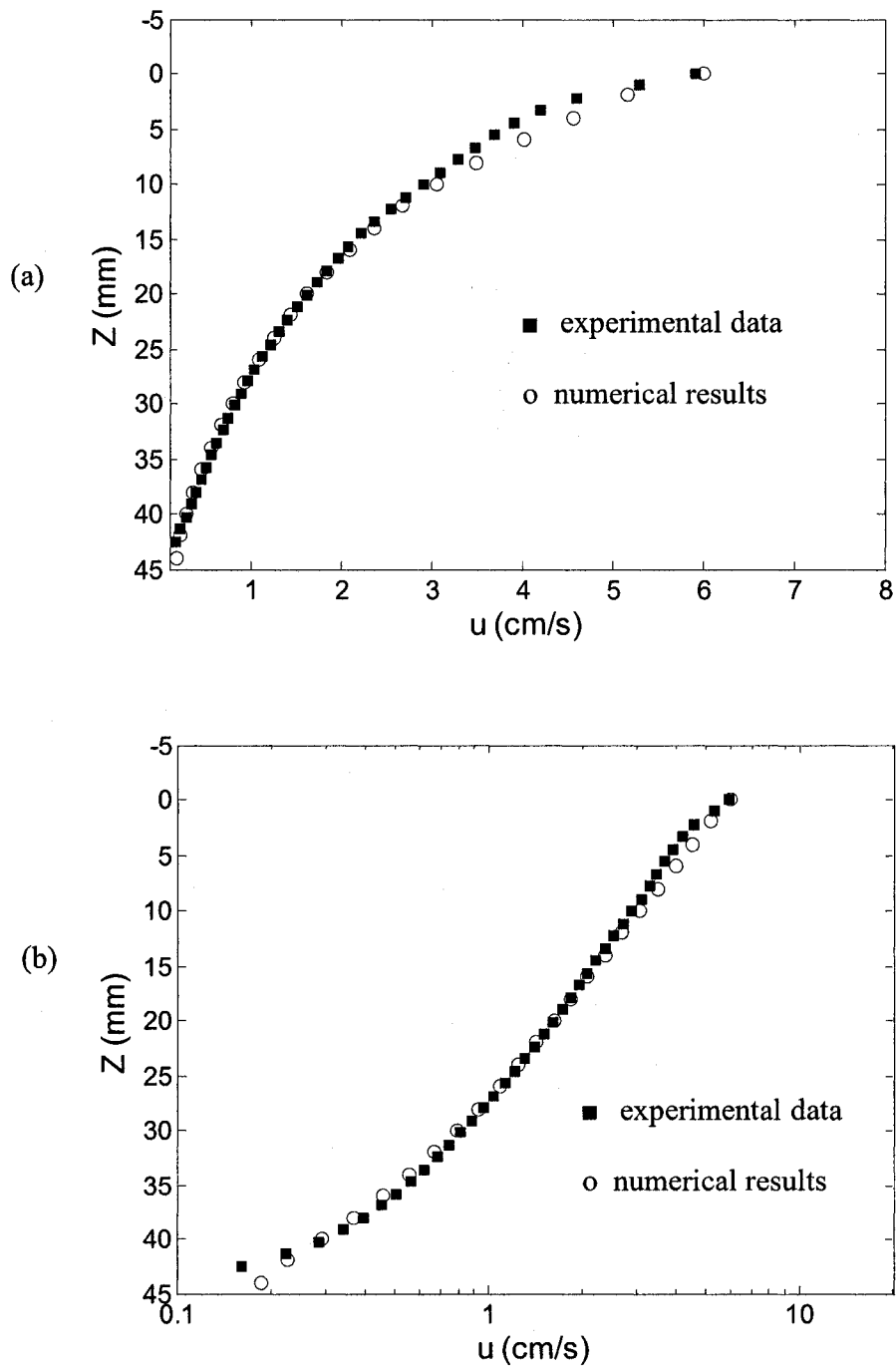


**Figure 3.3:** Mean streamwise velocity profiles at a wind speed of  $4.4 \text{ m} \cdot \text{s}^{-1}$ . (a) linear scale; (b) semi-logarithmic scale. ( $Z=0$  represents the water surface)

# **Chapter IV**

## **Results and Discussions**

### **4.1 Two-Dimensional Simulations**

#### **4.1.1 Clean Surface Condition**

The instantaneous velocity fields obtained from the numerical simulation and experimental studies are plotted in Figure 4.1. It can be easily seen from Figures 4.1a and 4.1b that the velocities just beneath the water surface are much larger than those at greater depths. Figure 4.2 plots the corresponding vorticity structure of the velocity field shown in Figure 4.1a. The figure shows that there is a strong vorticity region near the water surface. Also, a series of strong counter-rotating vorticities are observed under the wave crest. This observation is consistent with previous experimental studies (Jokardris 2004 and Siddiqui, 2002).

As mentioned in Chapter one, parasitic capillary waves riding along the forward face of the water crest have been observed in previous experimental studies. However, our numerical simulations did not capture the phenomenon of capillary waves riding along the forward face. There are two major reasons that may cause this problem: One reason is that the grid size (2mm) used in the simulation is not small enough; secondly, this might be due to the fact that the gas phase is not directly solved along with the liquid phase.

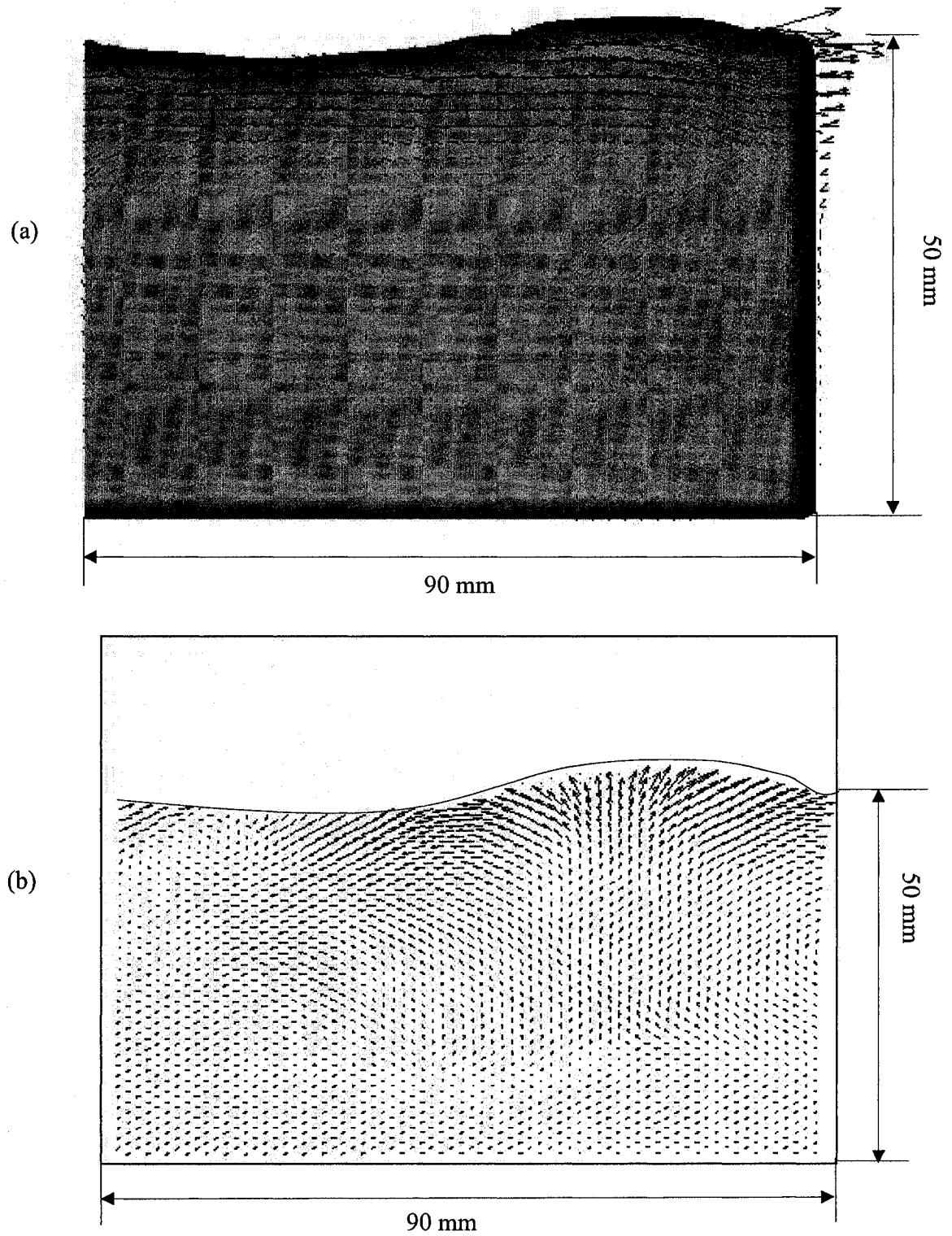


**Figure 4.1:** A typical field of velocity vectors obtained from (a) numerical simulation; (b) experimental data

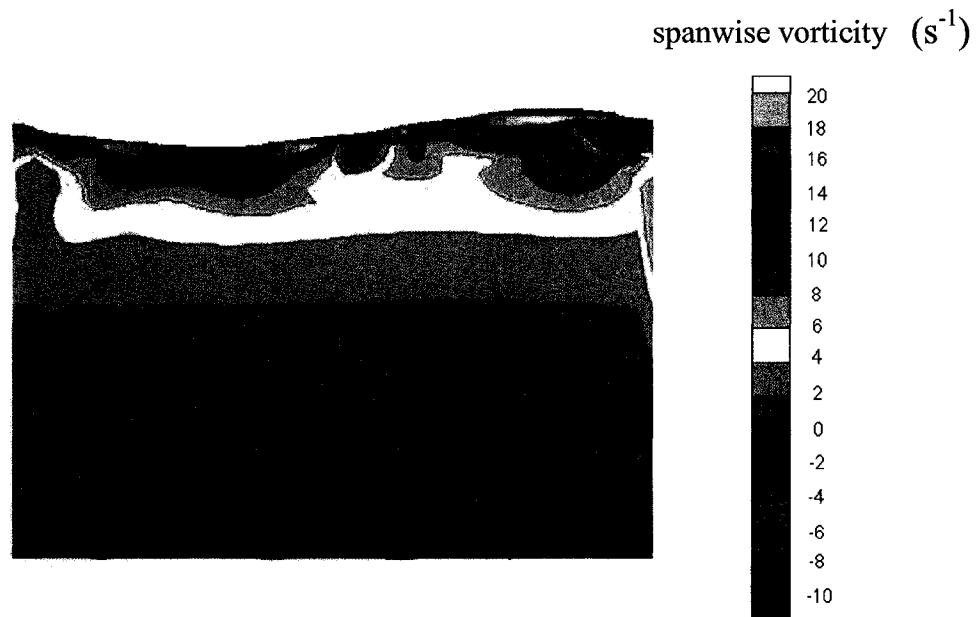


**Figure 4.2:** *A typical field of vorticity obtained from numerical simulation*

Figure 4.3 illustrates the mean velocity profiles corresponding to three different wind speeds. The zero level of the depth in this figure is set at the air-water interface. The velocities obtained from the numerical simulation are transformed with respect to the water surface. At a given wind speed, the results yield a decrease in the mean streamwise velocity with an increase in depth. For example, at a wind speed of  $3.6m \cdot s^{-1}$ , the mean streamwise velocity at the surface is  $5.0cm \cdot s^{-1}$ . The velocity drops to  $2.3cm \cdot s^{-1}$  at the depth of 10mm, and with a further decrease in depth to 20mm, it drops to  $1.126cm \cdot s^{-1}$ . The velocity approached to zero at the depth of 50mm due to the no slip boundary condition imposed at the bottom of the simulated tank. The figure also shows that the mean streamwise velocity increased with an increase in wind speed.

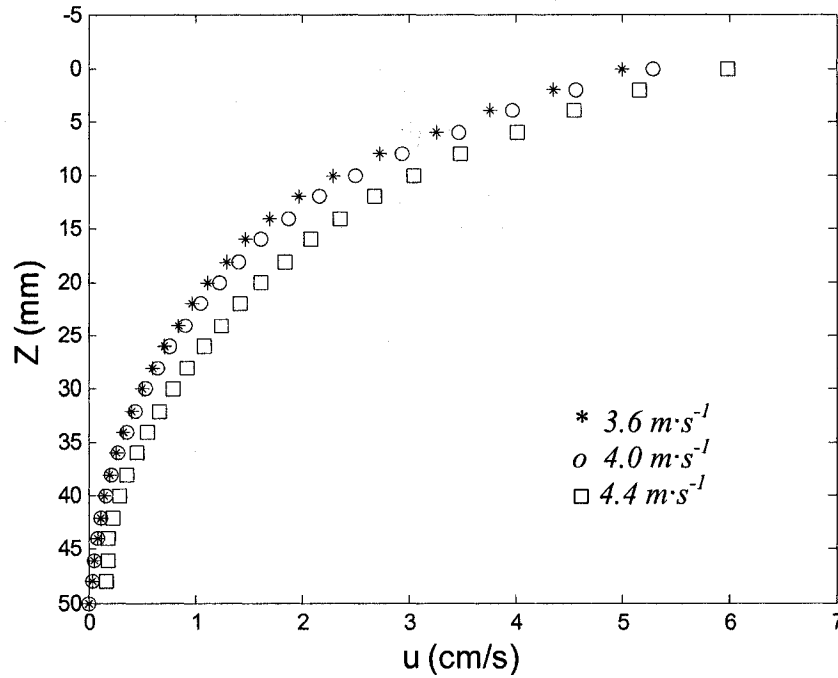


**Figure 4.3:** Mean streamwise velocity profile obtained from numerical simulations for different wind speed.

The mean streamwise velocities at five different depths and three different wind speeds are listed in Table 4.1. The results show that the mean streamwise velocity is  $5.00\text{cm}\cdot\text{s}^{-1}$  at the surface for a wind speed of  $3.6\text{m}\cdot\text{s}^{-1}$ . This velocity has an increase of 9.3% at a wind speed of  $4.0\text{m}\cdot\text{s}^{-1}$ . When the wind speed increases from  $3.6$  to  $4.4\text{m}\cdot\text{s}^{-1}$ , the surface velocity increased by 20%. Similar increasing trends for velocity with respect to wind speed are found in various depths. It is also shown by Table 4.1 that when the wind speed is between  $3.6\text{m}\cdot\text{s}^{-1}$  and  $4.4\text{m}\cdot\text{s}^{-1}$ , the surface velocity is approximately 1.4 % of the wind speed. The result agrees well with the experimental study conducted by Peltson (1997), which shows that the surface velocity was approximately 1-2% of the wind speed.

**Table 4.1:** the mean streamwise velocities ( $\text{cm}\cdot\text{s}^{-1}$ ) corresponding to different depths and different wind speed

<div style="display: inline-block; transform: rotate(-45deg);"> wind speed (<math>\text{m}\cdot\text{s}^{-1}</math>) depth (mm) </div>	3.6	4.0	4.4
0	5.00	5.47	6.00
10	2.31	2.60	3.05
20	1.13	1.27	1.63
30	0.51	0.56	0.79
40	0.19	0.17	0.29

Previous studies have already demonstrated that the velocity profile of a turbulent flow is composed of an inner, an outer layer, and an intermediate buffer layer (see White, 1991). The inner layer is the region dominated by the viscous shear, while the outer layer is the region dominated by the turbulent shear. The overlap layer refers to the region that is influenced by both viscous shear and turbulent shear and is considered as a smooth connection between the inner and outer regions. The velocity-defect law was used to plot the profile of mean streamwise velocity distribution normalized by wall coordinates, which is given as:

$$u^+ = \frac{U_s - u(z)}{u_*} \quad (4.1)$$

$$z^+ = \frac{u_* z}{\nu} \quad (4.2)$$

where,  $U_s$  is the mean streamwise velocity at the surface;  $u_*$  is the friction velocity;  $\nu$  is the kinematics viscosity and  $z$  is the distance from the water surface. The friction velocity  $u_*$  was calculated by a first order difference equation,

$$u_* = \sqrt{\nu \frac{U_s - U_{s-\Delta z}}{\Delta z}} \quad (4.3)$$

Here,  $\Delta z$  is the grid size in the  $z$  direction and  $U_{s-\Delta z}$  is the mean streamwise velocity of the cell immediately below the surface cell. The friction velocities calculated by Equation 4.3 are shown in Table 4.2 with respect to wind speed. The results indicate that the friction velocity varies from 1.80 to 2.03  $\text{mm}\cdot\text{s}^{-1}$  as the wind speed increases from 3.6 to 4.4  $\text{m}\cdot\text{s}^{-1}$ , which is consistent with the previous experimental study (Siddiqui & Loewen 2007).

**Table 4.2:** the friction velocity  $u_*$  at a function of wind speed

Wind speed ( $\text{m}\cdot\text{s}^{-1}$ )	Friction velocity $u_*$ ( $\text{mm}\cdot\text{s}^{-1}$ )
3.6	1.80
4.0	1.94
4.4	2.03

The mean streamwise velocity distribution in the form of the velocity-defect law is presented in Figure 4.4 for three wind speeds. The results indicate the existence of the viscous sublayer near the water surface at  $z^+ \leq 5$ . In this layer the velocity profile is linear and satisfies the relation of  $U^+ = z^+$ . Furthermore, Figure 4.3 shows the overlap region when  $60 \leq z^+ \leq 100$ , which is consistent with White (1991). The overlap region again provides evidence to the logarithmic distribution of mean streamwise velocity.

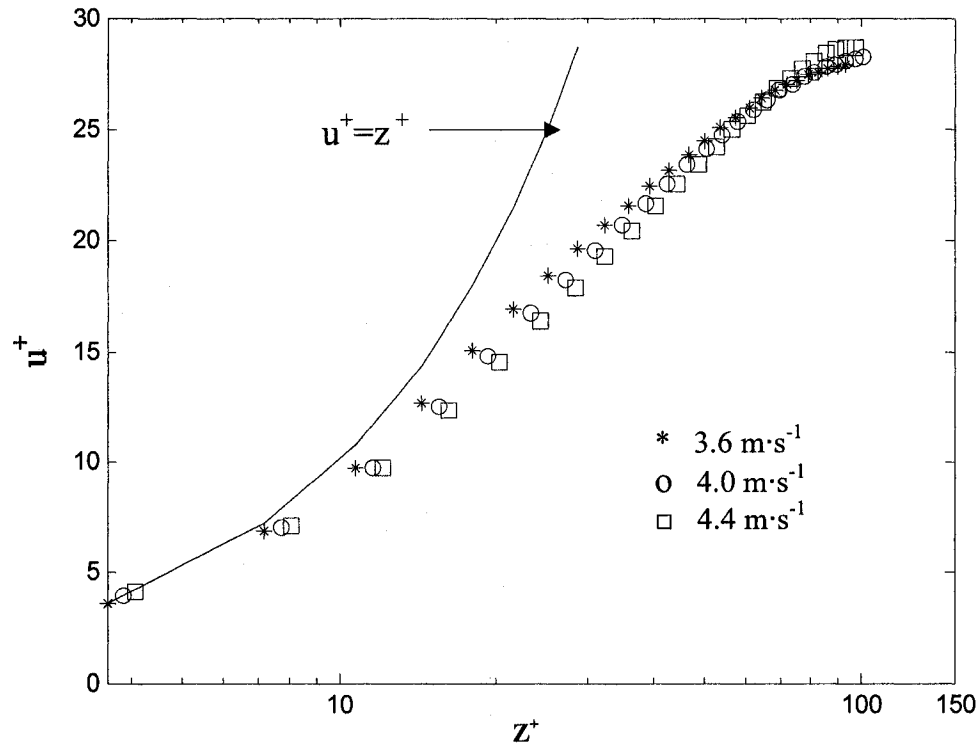


**Figure 4.4:** Semi-log mean streamwise velocity profile plotted in the form of the velocity defect law in wall coordinates.

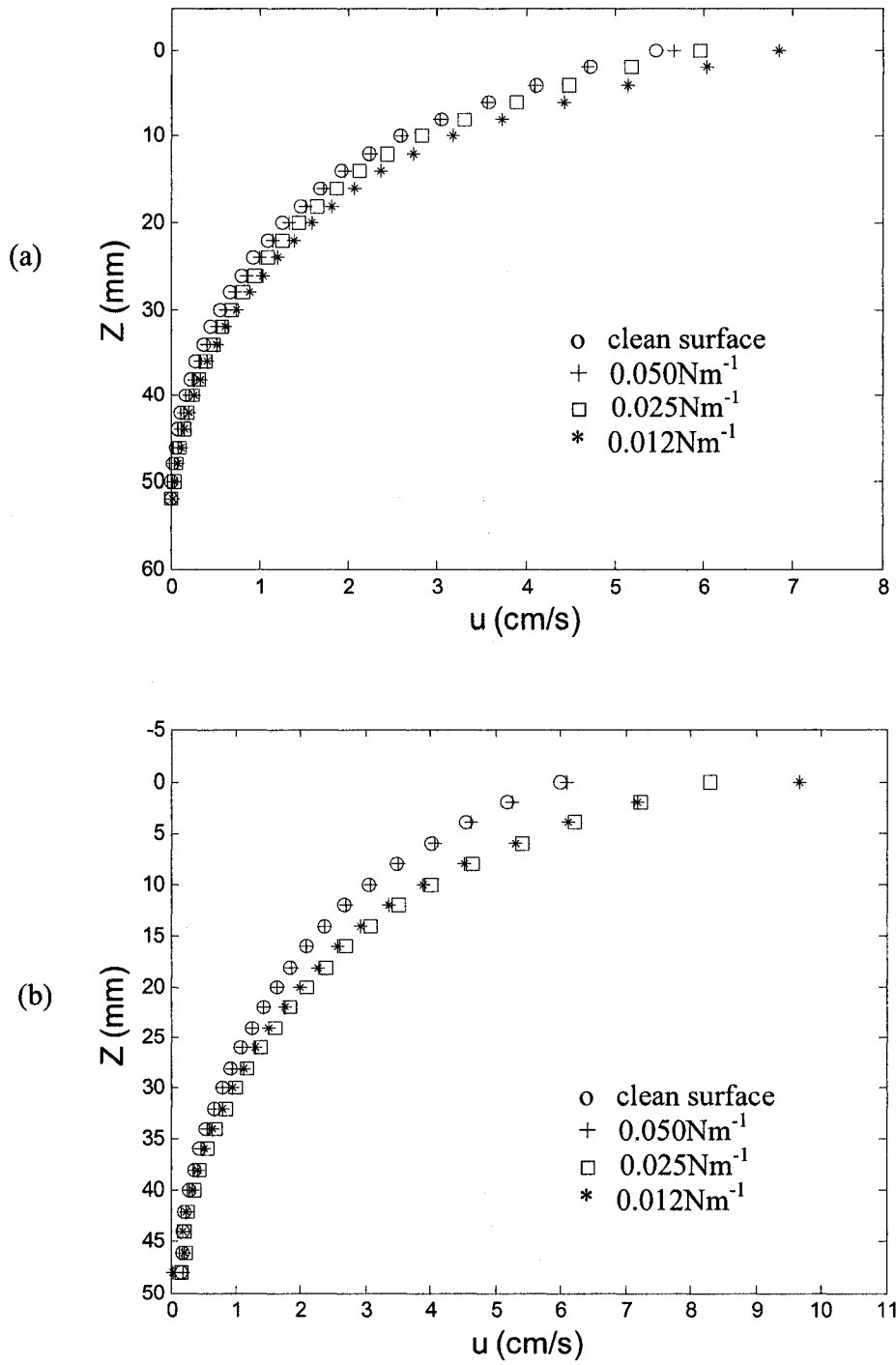
#### 4.1.2 Effect of Surface Contamination

Surface contamination is a serious environmental issue for oceans and lakes. Previous studies have shown that it plays an important role in the process of heat and gas exchange between air and water. It has also been demonstrated that the surface contamination tends to lower the surface tension and surfactant also dampens small scale waves (Jokardris 2004, Kamash 2005, Lang and Gharib 2000). In the case without wind blowing, the surface tension is the only surface stress acting at a clean air-water interface. Surface contaminations or surfactants tend to reduce the surface tension proportionally to their concentration at the free surface. Therefore, when the surfactant concentration varies along a free surface, surface tension gradients generate. The formation of surface tension



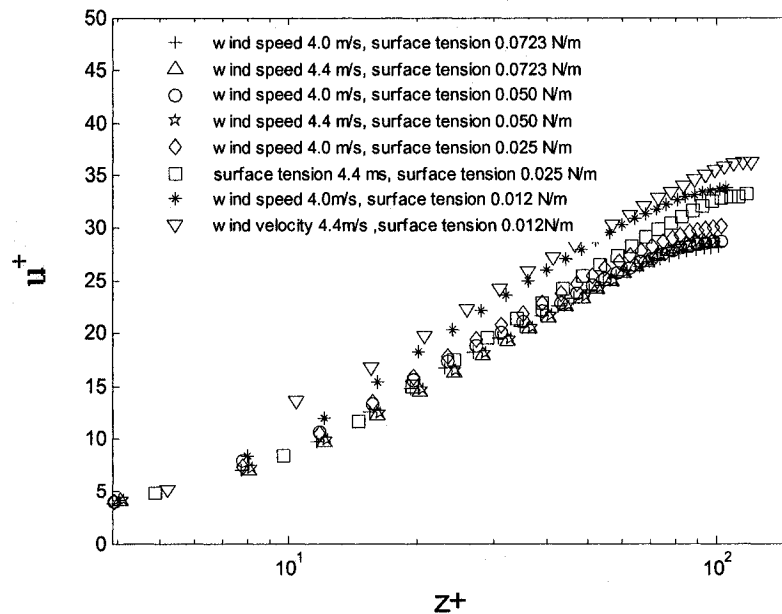
gradients produces shear stresses at the free surface, and then changing the surface boundary conditions. In this study, we investigate the effect of surface contaminations by reducing the surface tension in the numerical model. As we mentioned in Chapter 2, the surface tension is modeled as a body force instead applied at the interfacial cells.

Figure 4.5 shows the mean streamwise velocity profile for different wind speeds and at various values of surface tension. The plots show that at a given level of surface contamination, the mean streamwise velocity increases with wind speed and decreases with depth. At a given wind speed, the mean streamwise velocity increases with an increase in surface contamination (i.e. a decrease in surface tension). At a wind speed of  $4.0 \text{ m}\cdot\text{s}^{-1}$ , the mean streamwise velocity just beneath the interface with surface tension of  $0.012\text{N}\cdot\text{m}^{-1}$  is 25% larger than that of a clean surface. This value is increased to 61% as the wind speed increased to  $4.4 \text{ m}\cdot\text{s}^{-1}$ . Jokardris (2004) experimentally investigated the impact of surfactants on the mean velocity field at wind speeds of  $6.3$  and  $8.1 \text{ m}\cdot\text{s}^{-1}$ . She also observed an increase in the near-surface mean velocity by 25-30% which is consistent with the present numerical results.



**Figure 4.5:** the mean streamwise velocity profiles for various surface tension and wind speeds of (a)  $4.0\text{m.s}^{-1}$ ; (b)  $4.4\text{m.s}^{-1}$ .

Figure 4.6 plots the mean streamwise velocity profile in the form of the velocity defect law. The results first demonstrate that the surface contaminations did not change the logarithmic velocity profile of the clean surface. The viscous sublayer which was described in 4.1.1 still exists when the water is contaminated. However, the figure shows that the surfactants have a great effect on the overlap region described in section 4.1.1. At a given wind speed, when the surface tension is decreased from  $0.0723\text{N}\cdot\text{m}^{-1}$  (for clean surface) to  $0.05\text{N}\cdot\text{m}^{-1}$  and then to  $0.025\text{N}\cdot\text{m}^{-1}$ , the velocity profiles for different surface tension are very close with each other, and an overlap region can be identified. However, when the surface tension is further decreased to  $0.012\text{N}\cdot\text{m}^{-1}$ , the velocity profile departs from others. The plot also shows that the velocity profile becomes smoother with an increase in surface contamination. This is likely due to the reason that the surfactant dampens small scale surface waves resulting in the smooth surface.



**Figure 4.6:** Semi-log mean streamwise velocity profile plotted in the form of the velocity defect law.

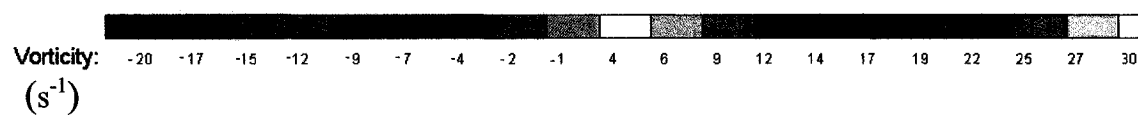
The effect of surface contaminations on wave characteristics is presented in Table 4.3. The results show that when the air-water surface is contaminated, the RMS amplitude decreases. For example, the RMS amplitude decreases approximately 28% (from 1.8mm to 1.2 mm) as the surface tension decreases from  $0.073\text{N}\cdot\text{s}^{-1}$  (clean surface) to  $0.012\text{N}\cdot\text{s}^{-1}$ . It also shows that the dominant wavelength is independent of surfactants. Similar effect of surfactants on these wave characteristics was observed in previous experimental studies (Jokardris 2004, Kamash 2005 and Zappa 1999).

**Table 4.3:** Wave characteristics with different surface tension at a wind speed of  $4.4\text{ m}\cdot\text{s}^{-1}$

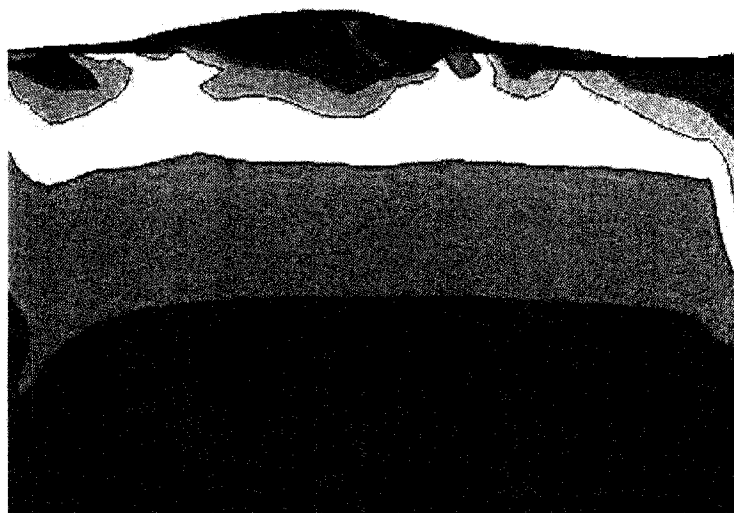
Surface tension ( $\text{N}\cdot\text{m}^{-1}$ )	RMS amplitude (mm)	Dominant wavelength (mm)
0.073 (clean surface)	1.8	90
0.050	1.6	90
0.025	1.3	90
0.012	1.2	90

Figure 4.7 presents the structure of vorticity at a wind speed of  $4.4\text{ m}\cdot\text{s}^{-1}$  for various degrees of water surface contamination. The structure of vorticity for clean surface is shown in Figure 4.7a. As mentioned in section 4.1.1, for clean surface, strong vorticities are distributed near the water surface and a series of strong counter-rotating vorticity are observed under the water crest. Figure 4.7b and c show the structure of vorticity for contaminated water surface with surface tensions of  $0.050$  and  $0.012\text{N}\cdot\text{m}^{-1}$ . These figures show that strong vorticities are still observed near the contaminated water surface. However, compared with the vorticities for the clean surface case, the strength of the

vorticity near the water surface becomes weak, especially the counter-rotating vorticities under the wave crest.



(a)



(b)



(c)

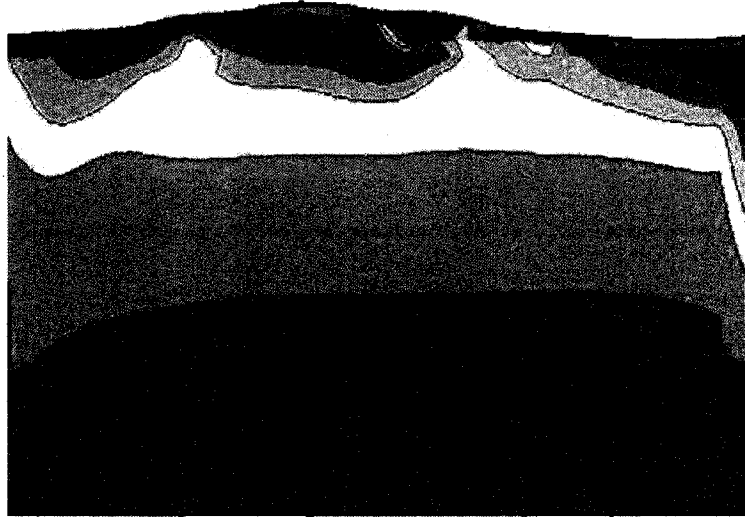


*Figure 4.7: Spanwise vorticity distribution at a wind speed of  $4.4\text{m}\cdot\text{s}^{-1}$  for various surface tensions (a)  $0.073\text{N}\cdot\text{m}^{-1}$  (clean surface); (b)  $0.050\text{N}\cdot\text{m}^{-1}$ ; (c)  $0.012\text{N}\cdot\text{m}^{-1}$ .*

## 4.2 Three-Dimensional Simulations

Wind-generated water waves are wide spread over the ocean surface and are three-dimensional in nature. Figure 4.8 shows a typical field image of the water surface (Banner and Peregrine 1993). The image shows small wave fronts which are three-dimensional and spread all over the image. The small-scale waves are likely the microscale breaking waves that do not entrain air. A large-scale breaking wave that entrained air and produced “white” cap is also visible in the upper left side of the image. Figure 4.9 shows a picture of wind-generated water surface taken from an experiment conducted at a low wind speed in a tank of  $3\text{m} \times 0.45\text{m} \times 0.9\text{m}$ . It can be clearly seen in this figure that some capillary waves ride along the frontage of the wind-generated wave. Also the three-dimensional effect can be observed in this image.



**Figure 4.8:** An area of wind blown water surface  $4\text{m} \times 3\text{m}$ , showing a small spilling breaker and a lot of microscale breaking (Banner & Peregrine 1993)



**Figure 4.9:** Wind-generated water waves taken from an experiment conducted in a tank of  $3\text{m} \times 0.45\text{m} \times 0.9\text{m}$

The subject of water waves has attracted a lot of researchers for many years now. Meiron (1982) numerically investigated the steady three-dimensional symmetric wave patterns of deep water gravity waves with finite amplitude by solving water-wave equations. The authors mentioned that the numerical results agreed well with the experimental observations. Guyenne *et al.* (2005) numerically investigated the shoaling and the breaking of solitary waves over a sloping ridge in a three-dimensional wave tank. Fully nonlinear potential flow equations expressed in a mixed Eulerian-Lagrangian form were solved in the numerical model using a method combined high-order boundary-element and explicit time-integration. The paper presented that three-dimensional effects were found on the time evolution, shape and kinematics of breaking waves due to the transverse modulation of the rigid topography. By comparison of two- and three-dimensional numerical results, the authors concluded that there were remarkable similarities in the shape and dynamics of the plunging breaker (a breaking wave whose crest curls over and collapses suddenly).

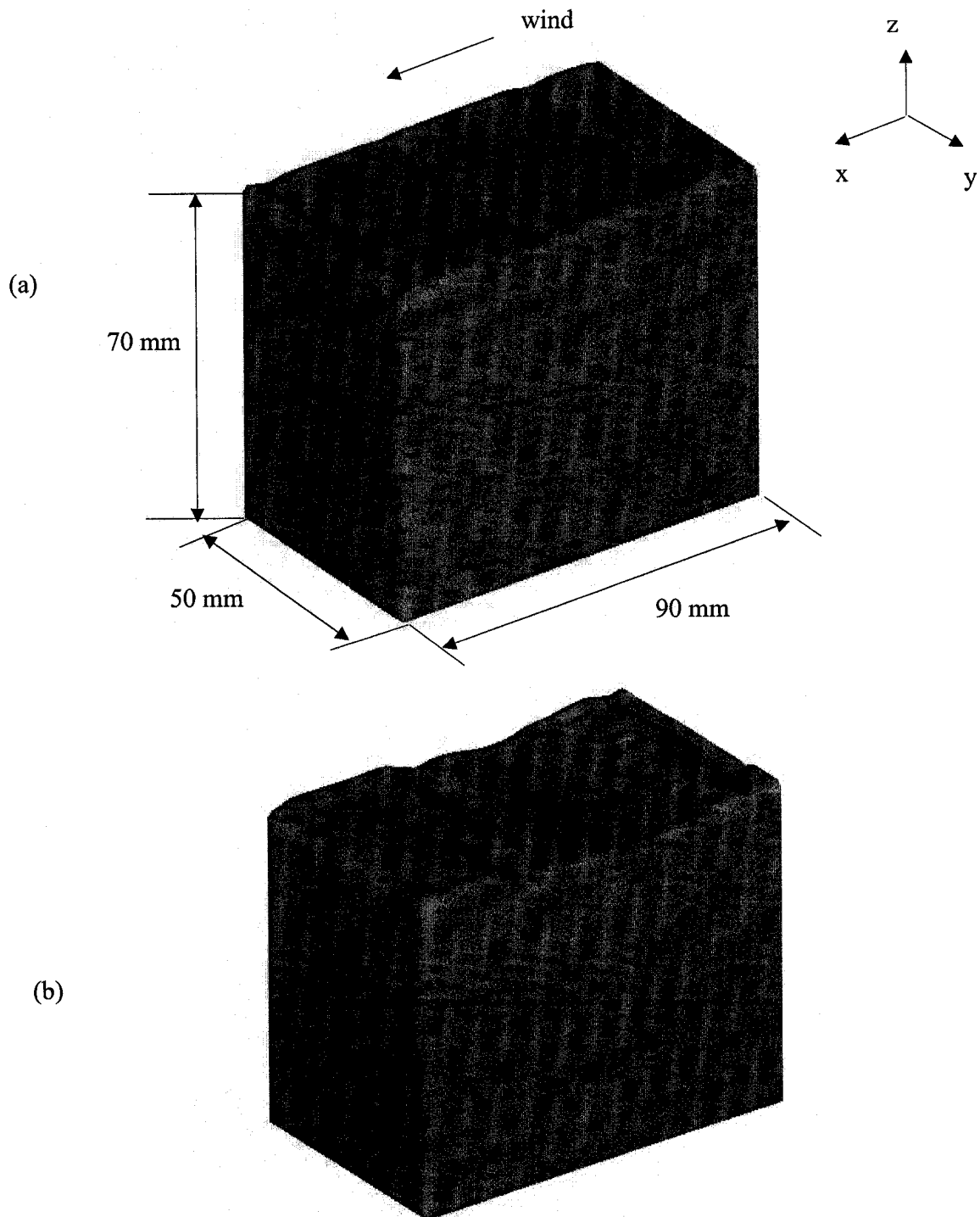
However, until now little research was found on the subject of three-dimensional small scale wind-driven water waves. The present research investigated the three-dimensional wind-driven water waves with small amplitude.

#### **4.2.1 Clean Surface Condition**

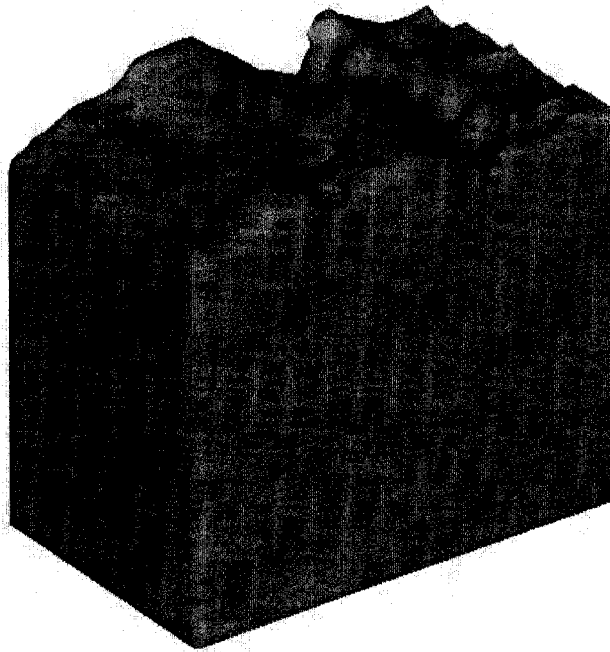
The three-dimensional wave generation process at a wind speed of  $3.6 \text{ m}\cdot\text{s}^{-1}$  is shown in Figure 4.10. The results indicate that the wind-driven water waves start as two-dimensional (Figure 4.10a), and after a short time, the three-dimensional effects appear (Figure 4.10b). Later, three-dimensional waves are generated in different regions of the



water surface (Figure 4.10c). Fully developed three-dimensional water waves are found in Figure 4.10d. Therefore, it can be concluded that the wind-driven waves start two-dimensional and then develops into three-dimensional waves quickly.



(c)



(d)

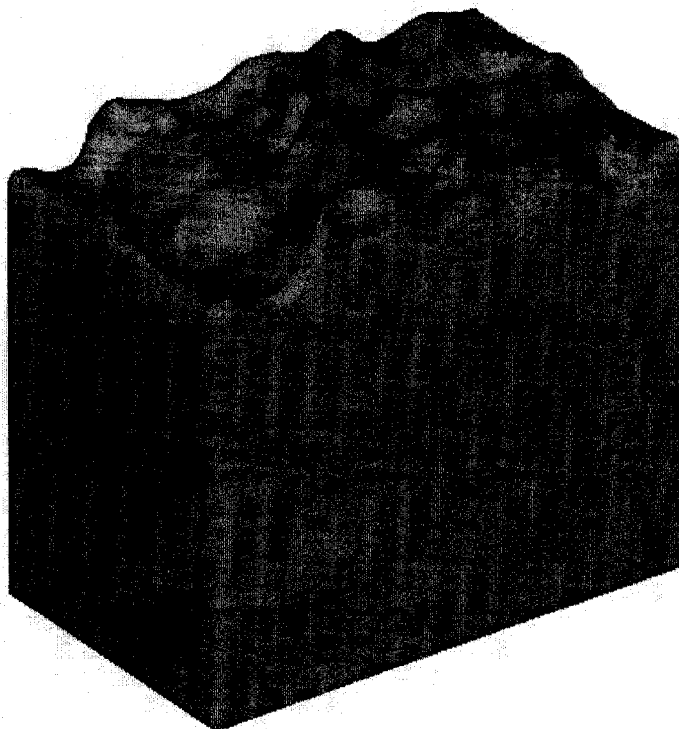


**Figure 4.10:** Three-dimensional wave generation at a wind speed of  $3.6 \text{ m}\cdot\text{s}^{-1}$ .  
(a) time = 0.26s; (b) time = 0.40s; (c) time = 0.50s; (d) time = 0.60s.

The wind-wave generation at a wind speed of  $4.4 \text{ m}\cdot\text{s}^{-1}$  is presented in Figure 4.11. It shows that when the wind speed is increased, the two-dimensional waves appear first and in a short time they develop into three-dimensional waves. The main difference of the wave generation process between a wind speed of  $4.4 \text{ m}\cdot\text{s}^{-1}$  and  $3.6 \text{ m}\cdot\text{s}^{-1}$  is that the time for the waves to be fully developed into three-dimensional waves is greatly shortened with an increase of wind speed.

Figure 4.12 demonstrates the structure of vorticity for clean surface at a wind speed of  $3.6 \text{ m}\cdot\text{s}^{-1}$  extracted from three-dimensional numerical simulations. The structure of y vorticity shown in Figure 4.12a is for the middle plane of the simulating tank in the y direction. Compared with the previous two dimensional results, the three-dimensional simulations show a significant change in y vorticity near the water surface. The strength of the vorticity calculated from the three-dimensional numerical simulation is much larger than that calculated from the two-dimensional analysis. In the two-dimensional case, the maximum vorticity is approximately  $20 \text{ s}^{-1}$ , however, this number increased to  $400 \text{ s}^{-1}$  for the three-dimensional case. Another difference between the two analyses is that the counter-rotating vorticities are distributed everywhere near the water surface for the three-dimensional simulation, however, for the two-dimensional simulation, this phenomenon is only observed under the wave crest. Figure 4.12b shows the extracted x-vorticity for the middle plane of the simulating tank. The counter-rotating vorticities are also observed near the water surface, which are responsible for the development of spanwise disturbances. However, the strength of the x-vorticities is weaker than that of the y-vorticity.

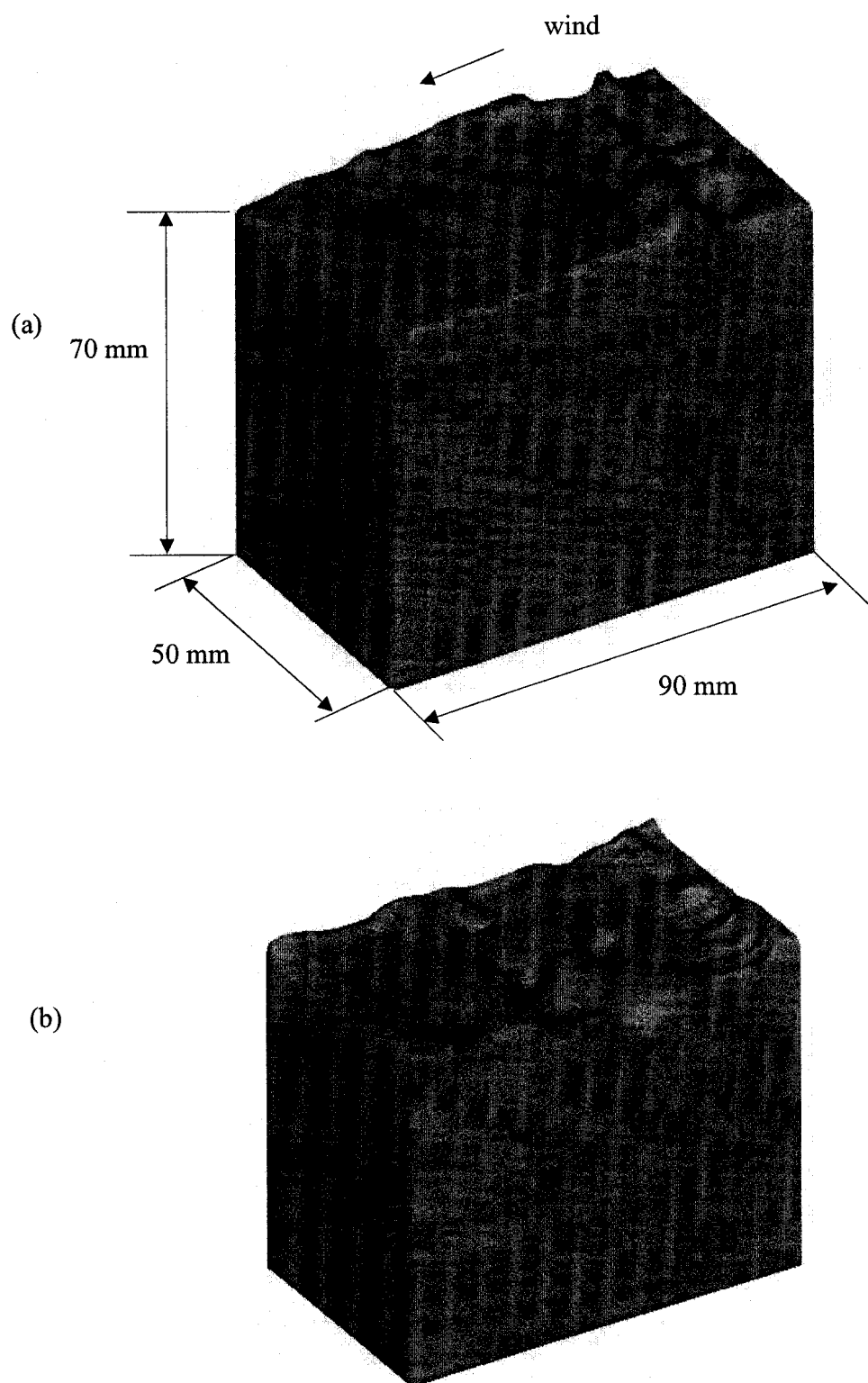


**Figure 4.11:** Three-dimensional wave generation at a wind speed of  $4.4 \text{ m}\cdot\text{s}^{-1}$ .  
(a) time = 0.2s; (b) time = 0.30s.

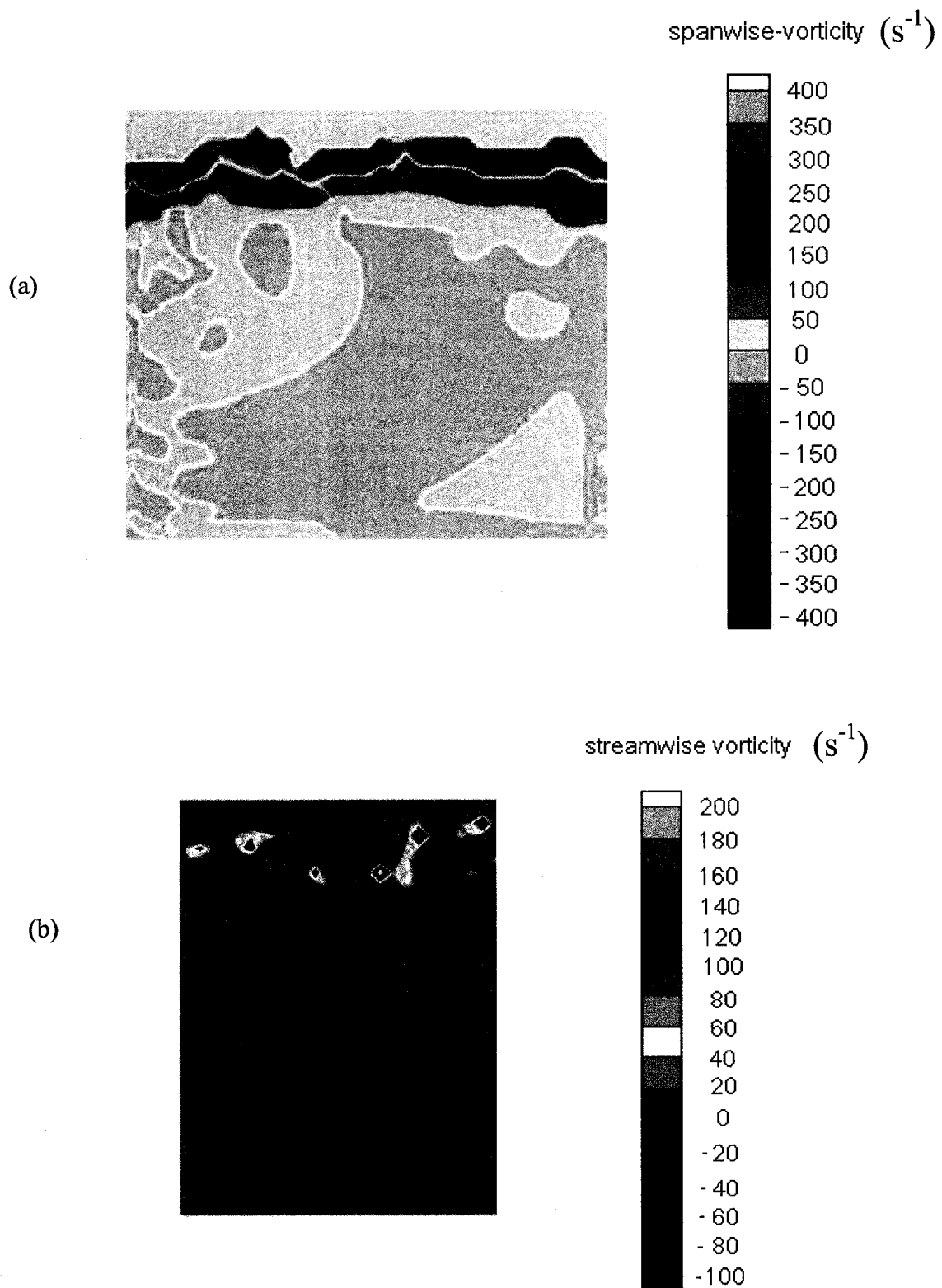
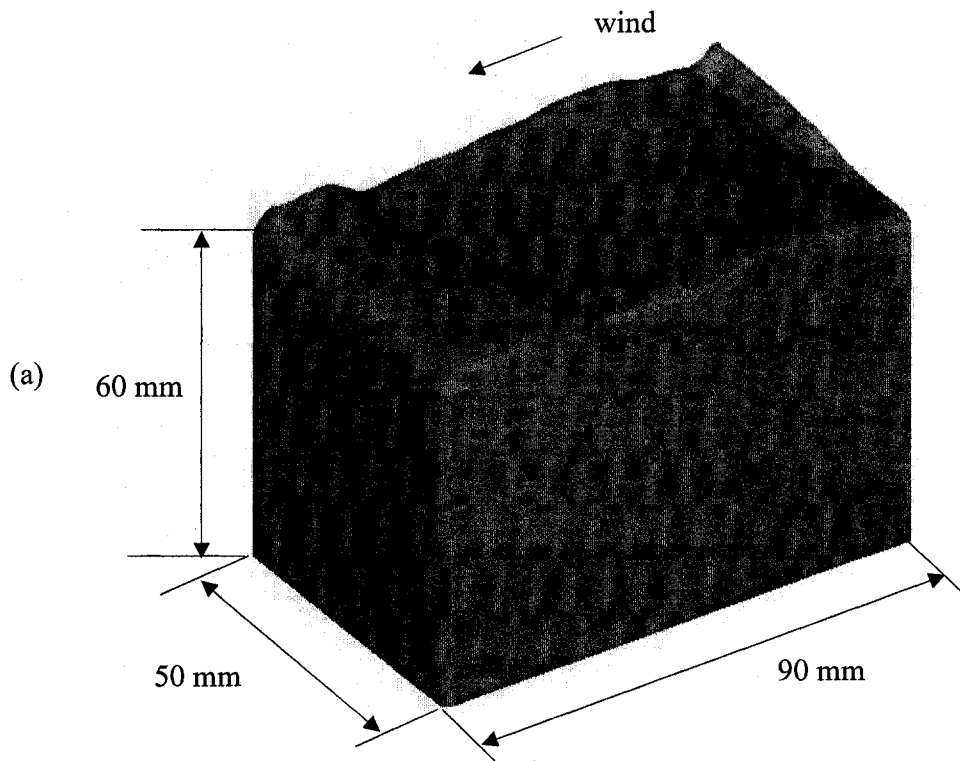


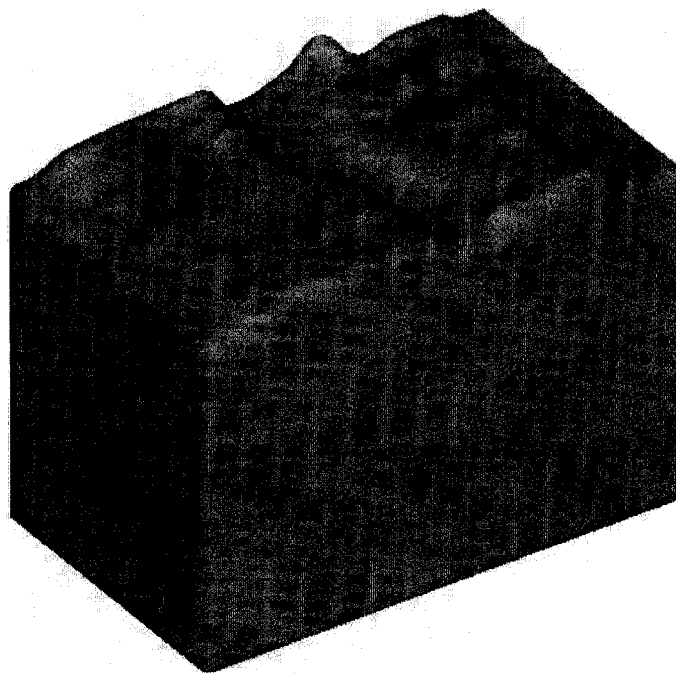
**Figure 4.12:** Structure of vorticity for clean surface at a wind speed of  $3.6m \cdot s^{-1}$   
 (a)spanwise- vorticity; (b)streamwise - vorticity.

#### 4.2.2 Effect of Surface Contamination on Wave Waves

The wind-driven water wave generating process at a wind speed of  $3.6 \text{ m}\cdot\text{s}^{-1}$  with a contaminated surface is shown in Figure 4.13. In this simulation, the effect of surface contamination is modeled using a surface tension of  $0.028 \text{ N}\cdot\text{m}^{-1}$ . Compared with the wave generation of a clean surface at the same wind speed (see Figure 4.10), the results show that the surface contamination delays the occurrence of the three-dimensional characteristics. For a clean surface, the three-dimensional effect starts to appear at  $0.4 \text{ s}$  when the wind speed is  $3.6 \text{ m}\cdot\text{s}^{-1}$  (see Figure 4.10b), and this time prolongs to  $0.5 \text{ s}$  with the condition of surface contamination at the same wind speed. Therefore, the total time used to fully generate three-dimensional waves delays when water surface was contaminated.



(b)



(c)

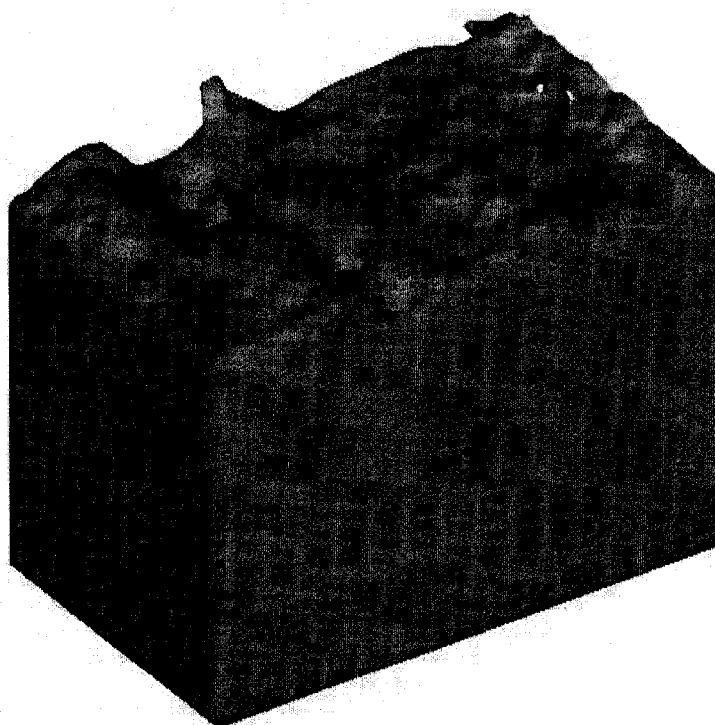
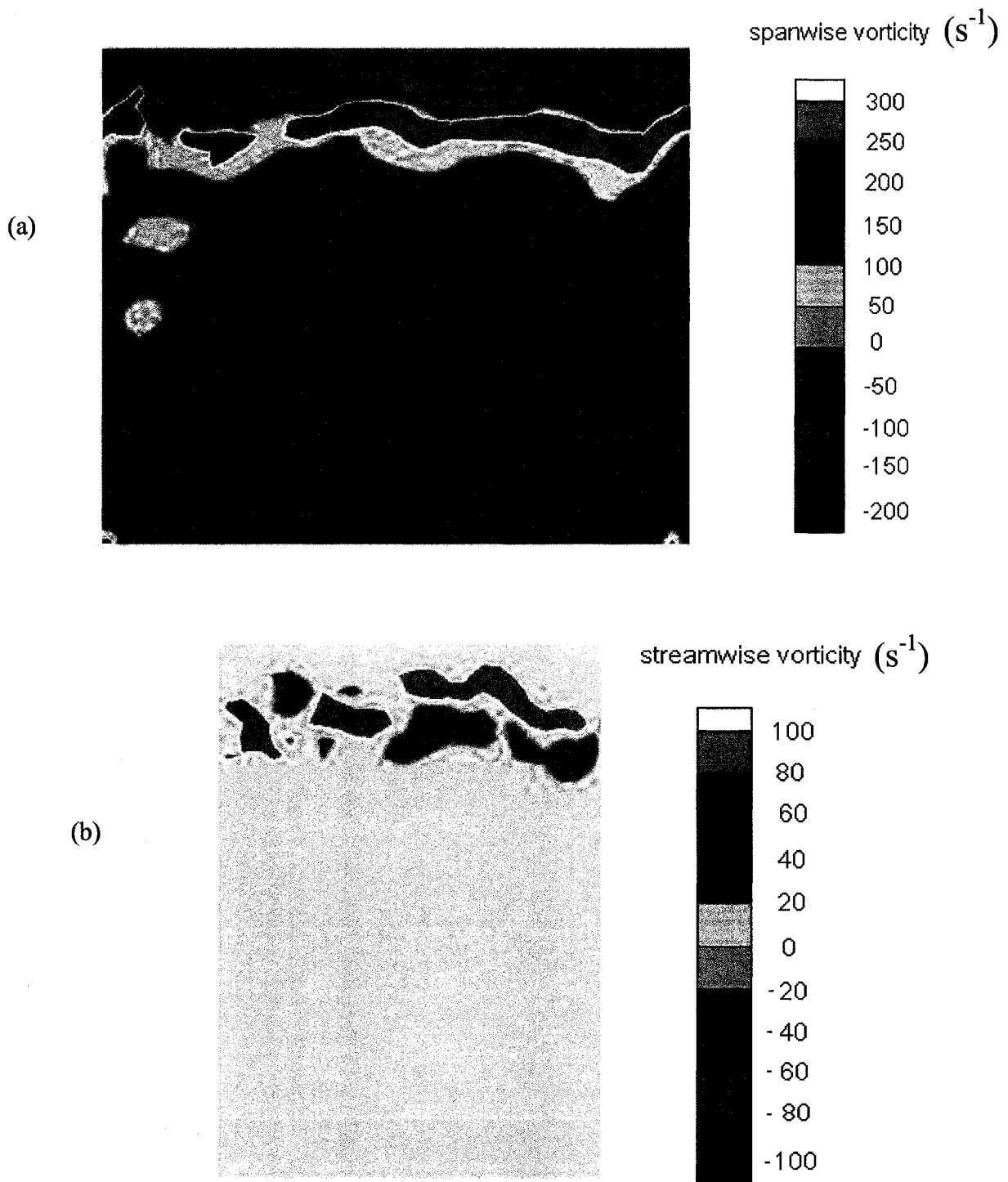


**Figure 4.13:** Three-dimensional wave generation at a wind speed of  $3.6 \text{ m}\cdot\text{s}^{-1}$  and surface tension of  $0.0228 \text{ N}\cdot\text{m}^{-1}$ . (a) time =  $0.50\text{s}$ ; (b) time =  $0.60\text{s}$ ; (c) time =  $0.70\text{s}$ .

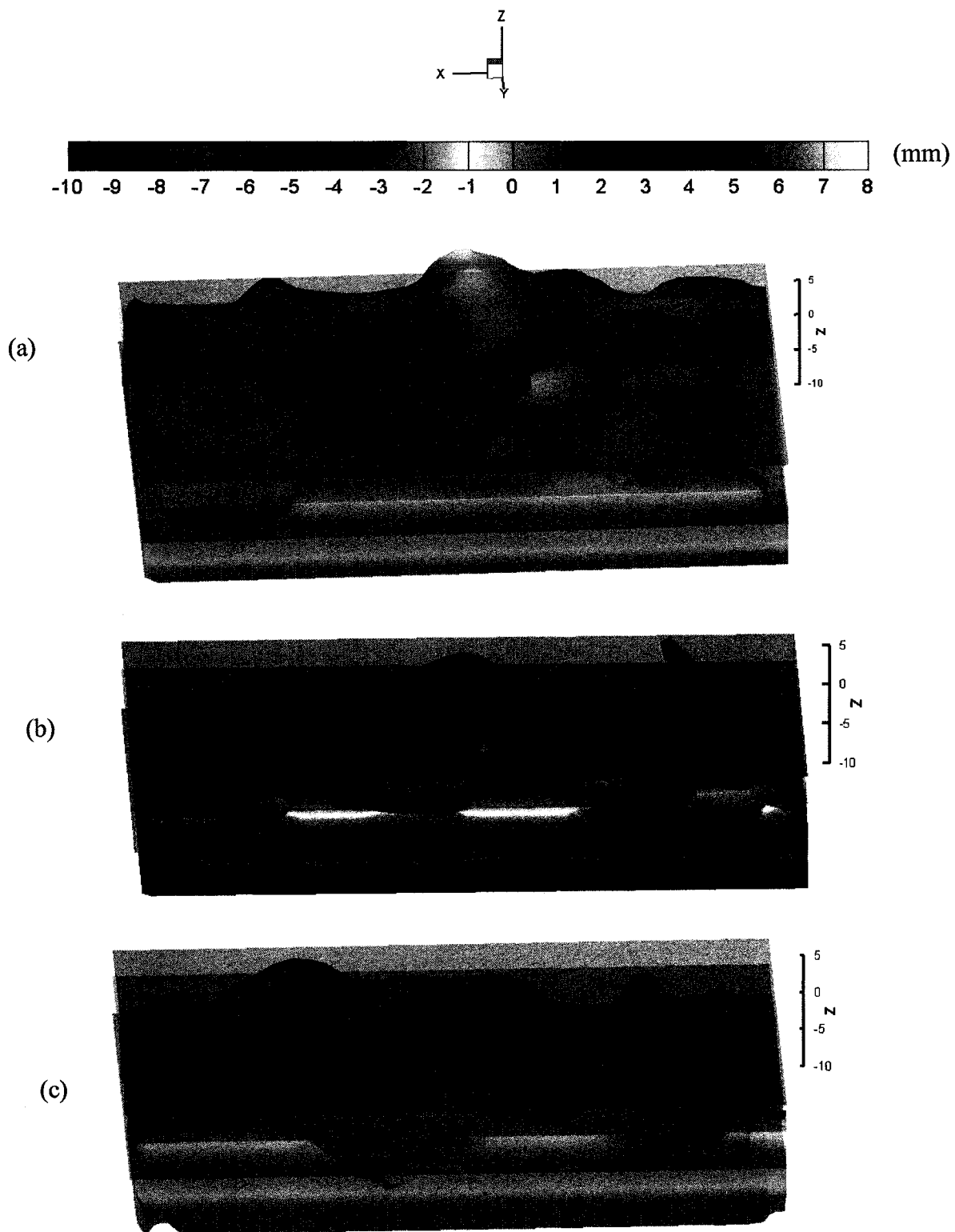
Figure 4.14 illustrates the structure of vorticity for contaminated water surface at a surface tension of  $0.05\text{N}\cdot\text{m}^{-1}$  and a wind speed of  $3.6\text{m}\cdot\text{s}^{-1}$ . The y-vorticity (Figure 4.14a) and the x-vorticity (Figure 4.14b) are extracted from the middle plane of the simulating tank in the y and x directions, respectively. The results show that the structure of the vorticity near contaminated water surface is similar to that of near clean surface. However, the strength of the vorticity near contaminated surface is different. The maximum clockwise y vorticity is  $300\text{s}^{-1}$  near contaminated water surface, but near clean surface, the maximum value is  $400\text{s}^{-1}$ . Similarly, the maximum counter-clockwise y-vorticity and clockwise x-vorticity of contaminated water surface are only 50% of those of the clean surface.

Figure 4.15 presents the water wave profiles at a wind speed of  $3.6\text{m}\cdot\text{s}^{-1}$  for different surface tensions at a time of 0.7 seconds. The mean water level (the middle layer) is set to zero as the datum. The upper layer refers to the layer 3 millimeter above the zero. Similarly, the lower layer refers to the layer 5 millimeter below the datum. The results showed that the maximum amplitude at the water surface decreased with a decrease in surface tension from  $0.0723\text{Nm}^{-1}$  to  $0.025\text{Nm}^{-1}$ . Therefore, an increase of concentration of the surface contaminants results in a decrease of the maximum amplitude of water surface.





**Figure 4.14:** Structure of vorticity for contaminated water surface at a surface tension of  $0.0228 \text{ N}\cdot\text{m}^{-1}$  and a wind speed of  $3.6 \text{ m}\cdot\text{s}^{-1}$  (a) spanwise-vorticity; (b) streamwise-vorticity.



**Figure 4.15:** Water surface profiles at a wind speed of  $3.6 \text{ m}\cdot\text{s}^{-1}$  and surface tension of (a)  $0.0723 \text{ N}\cdot\text{m}^{-1}$  (clean surface); (b)  $0.050 \text{ N}\cdot\text{m}^{-1}$ ; (c)  $0.025 \text{ N}\cdot\text{m}^{-1}$ .

# Chapter V

## Conclusion and Recommendation

### 5.1 Conclusion

Previous studies have shown that microscale wave breaking has a significant effect on the process of heat, gas, and energy exchange between water and air. Some experimental studies have been conducted to investigate the flow field beneath microscale breaking waves and their impact on the air water heat and mass transfer. However, there have been very few numerical studies on small-scale wind-driven water waves due to the three-dimensional nature of the flow and flow interactions between water and air. In this thesis, the numerical analysis of near-surface flow beneath small-scale wind driven water waves were studied.

In order to estimate the effect of wind on water waves, a gas model based on the experimental results of Dattatri *et al.* (1977) was developed. The developed gas model was a function of the friction velocity, free stream gas velocity, and kinematic viscosity of air. The friction velocity in this model was a function of wind speed and validated by previous experimental data. The average difference of the friction velocity obtained from the numerical and experimental studies was less than 10% for range of wind speeds from 2 to  $5\text{ m}\cdot\text{s}^{-1}$ . The gas model was also validated by previous experiments (Nasiruddiu and Siddiqui 2007). The results showed that the differences of wind velocities near the water surface between these two were less than 10% and the gas model works well at wind speeds that range from  $3\text{ m}\cdot\text{s}^{-1}$  to  $5\text{ m}\cdot\text{s}^{-1}$ .

Experiments were conducted at a wind speed of  $4.4 \text{ m}\cdot\text{s}^{-1}$  to validate the numerical model. The results showed a good agreement between the numerical and experimental results. In the region immediately below the water surface, the simulated velocities were slightly higher in magnitude than the experimental ones. The overall difference between these two is 2% based on the average velocity of the numerical and experimental results. The maximum difference is 6.78%, located at approximately 8 mm below the water surface. Moreover, the numerical model accurately estimated the wave characteristics of the near-surface flow beneath small-scale wind waves. The model also captured the logarithmic behavior of the mean streamwise velocity, which is consistent with the previous studies (Siddiqui *et al.* 2004; Siddiqui & Loewen 2007; Cheung *et al.* 1988). The results of the instantaneous velocity fields from the numerical simulation showed the existence of reverse velocity fields at greater depths, which also agreed well with the experimental studies. However, the numerical simulations did not capture the characteristic of capillary waves located at the forward face of a wave and strong turbulence just under the crest, which was found in the experimental study.

The two-dimensional results of the clean surface showed that the mean streamwise velocity at a given wind speed decreased with an increase of depth (the zero level was set at the interface at the initial condition). When the wind speed was increased from  $3.6 \text{ m}\cdot\text{s}^{-1}$  to  $4.4 \text{ m}\cdot\text{s}^{-1}$ , the mean streamwise velocity increased approximately 20% at the surface and similar increasing trends were found at all depths. The dimensionless velocity profile in wall coordinate which was obtained using the velocity-defect law indicated the existence of the viscous sublayer near the water surface at  $z^+ \leq 5$ . In this layer,  $U^+$  has a linear relation with  $z^+$  ( $U^+ \approx z^+$ ). The velocity-defect law profile also showed an overlap

region used to smoothly connect the inner and the outer regions of the turbulent flow at  $60 \leq z^+ \leq 100$ . The structure of vorticity extracted from two-dimensional numerical simulations showed that strong vorticity region exists near the clean water surface and a series of counter-rotating vorticities were observed under the wave crest.

Previous studies have shown that the surface condition (clean or contaminated) have a great effect on the wave field and heat and gas exchange between air and water. The two-dimensional results of contaminated surface showed that the surface contamination increased the mean streamwise velocity. This is consistent with the experimental investigation conducted by Jokardris (2004) on the impact of surfactants. It was also found that the velocity profile becomes smoother with an increase in surface contamination. The results of the structure of vorticity show that strong vorticities are still observed near the contaminated water surface. However, compared with the vorticities for the clean surface case, the strength of the vorticity near the contaminated water surface becomes weak, especially the counter-rotating vorticities under the wave crest.

In this study, some preliminary results of three-dimensional wind-driven water waves with small amplitude were presented. From these results, it can be concluded that the wind-driven waves started with two-dimensional waves and developed into three dimensional in a very short time. The transition time between two-and three-dimensional waves were shortened with an increase in wind speed.

The results of the three-dimensional simulations with surface contamination showed that the existence of contaminants delays the time for water waves to be fully developed into three dimensional waves. Also, surfactants reduced the maximum amplitude of the wave

profile. The results also show that the structure of the vorticity near contaminated water surface is similar to that of near clean surface. However, the strength of the vorticity near contaminated surface becomes weaker.

## **5.2 Recommendation for Future Research**

There are a few issues that could be further investigated.

- 1) In order to extend the application of the numerical results, it is strongly recommended to modify the gas model which is suitable to a larger range of wind speeds.
- 2) The capillary wave is an important characteristic in the process of wave generation. However, in this study, especially in the two-dimensional simulation, it can be seen that capillary waves were obviously not captured. Therefore, it is recommended to modify the model in order to capture the characteristic of capillary waves.
- 3) The wave and wave breaking are three-dimensional in nature. Therefore, a three-dimensional simulation is the final goal of our numerical analysis. Only the preliminary results of three-dimensional waves were presented in this thesis. More three-dimensional simulations that can be quantitatively compared with two-dimensional numerical results and experimental data are recommended to be conducted in the future.
- 4) The instability of three-dimensional simulations will also be worth deeper investigation.

**Reference:**

- Agüí, J.C. & Jiménez, J., "On the performance of particle tracking" *J. Fluid Mech.* **185**, 47-468, 1987
- Banner M. L. and Peregrine D.H., "Wave breaking in deep water" *Annu. Rev. Fluid Mech.* **25**, 373-397, 1993
- Banner M. L., and Phillips O. M., "On the incipient breaking of small scale waves" *J. Fluid Mech.* **65**, 647-656, 1974
- Brackbill J.U., Kothe D.B., and Zemach C., "A continuum method for modeling surface tension" *Theoretical Division, Los Alamos National Laboratory* 87545
- Bussmann M., Mostaghimi J. and Chandra S., "On a three-dimensional volume tracking model of droplet impact" *Physics of fluid*, **11**, 1406-1417, 1999
- Ceniceros H. D., "The effects of surfactants on the formation and evolution of capillary waves", *Physics of Fluids*, **15**, 245-256, 2003
- Chen G. and Kharif C., "Two-dimensional Navier-Stokes simulation of breaking waves" *Phys. Fluids*. **11**, 121-133, 1999
- Cheung T. K. and Street R. L., "The turbulent layer in the water at an air-water interface." *J. Fluid Mech.* **194**, 133-151, 1988
- Chu C. R. and Jirka G. H., "Reaeration in combined wind/stream driven flows in air-water gas transfer" edited by Jähne and E. C. Monahan, AEON Verlag and Studio, Hanau, Germany, 79-88, 1995
- Cowen E.A. and Monismith S.G., "A hybrid digital particle tracking velocimetry technique" *Exp. Fluids* **22**, 199-211, 1997

- Dabiri D. and Gharib M., "Experimental investigation of the vorticity generation within a spilling water wave" *J. Fluid Mech.* **330**, 113-139, 1997
- Dalrymple R. A. and Rogers B. D., "Numerical modeling of water waves with the SPH method" *Coastal engineering* **53**, 141-147, 2006
- Dattatri J., Jothi Shankar N. and Raman H., "Wind velocity distribution over wind-generated water waves" *Coastal Engineering* **1**, 243-260, 1977
- Duncan J. H. and Smith H., "Spilling breakers" *Ann. Rev. Fluid Mech.* **33**, 519-547, 2001
- Emerson S., "Seasonal oxygen cycles and biological new production in surface waters of the subarctic Pacific Ocean" *J. Geophys. Res.*, **92**, 6535-6544, 1987
- Ferziger J. H. and Perić M., "Computational methods for fluid dynamics" Springer Berlin, 1997
- Fincham A. M., and Spedding G. R., "Low cost, high resolution DPIV for measurement of turbulent fluid flow" *Exp. Fluids* **23**, 449-462, 1997
- Gotoh H. and Sakai T., "Lagrangian simulation of breaking waves using particle method" *Coastal engineering* **41**, 303-326, 1999
- Guyenne P. and Grilli S. T., "Numerical study of three-dimensional overturning waves in shallow water", *J. Fluid Mech.* **547**, 361-388, 2006
- Harlow F. H. and Welch J. E., "Numerical calculation of time-dependent viscous incompressible flow of fluid with free surface" *Physics of Fluids*, **8**, 2182-2189, 1965
- Hirt C.W. and Nichols B.D., "Volume of fluid method for dynamics of free boundaries" *J. Comput. Phys.* **39**, 201-225, 1981
- Jessup A.T., Zappa C.J. and Yeh Harry, "Defining and quantifying microscale wave breaking with infrared imagery", *J. Geophys. Res.* **102**, C10, 23145-23153



- Jokardris M., "Analysis of near-surface flow measurements beneath clean and contaminated wind-driven water surfaces" M.A.Sc Thesis, Mechanical and Industrial Engineering, Concordia University, 2004
- Jones I. S. and Toba Y., "Wind stress over the ocean" Cambridge University Press, 2001
- Kamash M.K.M.E. "The effect of surfactants on microscale wave breaking and the aqueous boundary layer" Ph.D. Thesis, Civil and Environmental Engineering, University of Alberta, 2005
- Kothe D. B., Mjolsness R. C. and Torrey M. D., "Ripple: A Computer Program for Incompressible Flows with Free Surfaces" Los Alamos National Laboratory, 1991
- Lang, A.L. and Gharib M., "Experimental study of the wake behind a surface-piercing cylinder for a clean and contaminated free surface" *J. Fluid Mech.* **402**, 109-136, 2000
- Marxen, M., "Particle image velocimetry in Strömungen mit starken Geschwindigkeitsgradienten" (Diplom Thesis) Fakultät für Physik und Astronomie, Ruprecht-Karls-Universität Heidelberg, 1998
- Mass J.T., Milgram, J. H. "Dynamic behavior of natural sea surfactant films". *J. Geophys. Res.* **103**, 15695-15715, 1998
- Meiron D.I., Saffman P. G. and Yuen, H. C., "Calculation of steady three-dimensional deep-water waves" *J. Fluid Mech.* **124**, 109-21, 1982
- Melville W.K. "The role of surface-wave breaking in air-sea interaction" *Ann. Rev. Fluid Mech.* **28**, 279-321, 1996

- Nichols B. D. and Hirt C. W., "Methods for calculating multi-dimensional, transient free surface flows past bodies" Proc. First Intern. Conf. Num. Ship Hydrodynamics, Gaithersburg, ML, Oct. 20-23, 1975
- Nithiarasu P., "An arbitrary Lagrangian Eulerian (ALE) formulation for free surface flows using the characteristic-based split (CBS) scheme", *Int. J. Numer. Meth. Fluids* **48**, 1415-1428, 2005
- Noh W. F. and Woodward P., "SLIC (simple line interface calculation)" Lecture Notes in Physics **59**, Springer, New York, 330-340, 1976
- Peirson W. L. and Banner M. L., "Aqueous surface layer flows induced by microscale breaking wind waves" *J. Fluid Mech.* **479**, 1-38, 2003
- Phillips O. M., "The dynamics of the upper ocean" Cambridge University Press, 1977
- Rapp R. J. and Melville W. K., "Laboratory measurements of deep-water breaking waves" *Phil Trans R Soc Lond*, **A331**, 735-800
- Rider W. J. and Kothe D. B., "Reconstructing volume tracking" *J. comput. Phys.* **141**, 112-152, 1998
- Shaikh N. and Siddiqui K., "Airside velocity measurement above the wind-generated water waves", 5<sup>th</sup> ASME-JSME Joint Fluids Engineering Conference, San Diego, CA, USA, July 31-August 2, 2007
- Siddiqui M.H. K., Loewen M. R., Richardson, C., Asher, W. E. & Jessup, A. T., "Simultaneous particle image velocimetry and infrared imagery of microscale breaking waves". *Physics of Fluids* **13**, 1891-1903, 2001

- Siddiqui M.H. K., "Laboratory Measurements of the Flow Beneath Microscale Breaking Waves", Ph.D. thesis, Department of Mechanical and Industrial Engineering, University of Toronto, 2002
- Siddiqui M. H. K., Loewen M. R., Asher W. E. and Jessup A. T. "Coherent structures beneath wind waves and their Influence on air-water gas transfer". *J. Geophys. Res.* **109**, C3, C03024, 2004
- Siddiqui M.H.K. and Loewen M.R. "Characteristics of the wind drift layer and microscale breaking waves" *J. Fluid Mech.* **573**, 417-456, 2007
- Terray E. A., Donelan M. A., Agrawal Y.C., Drennan W. M., Kahama K. K., Williams III A. J., Hwang P. A. and Kitaigorodskii S. A., "Estimates of kinetic energy dissipation under breaking waves" *J. Phys. Oceanogr.* **26**, 792-807, 1996
- White Frank M., "Viscous Fluid Flow" Second edition, McGraw-Hill, Inc. 1991
- Willert C. E. and Gharib M. "Digital particle image velocity" *Exp. Fluids* **10**, 181-193, 1991
- William L. Peltson, "Measurement of surface velocities and shears at a wavy air-water interface using particle image velocimetry", *Exp. Fluids* **23**, 42-437, 1997
- Youngs D.L., "Time-dependent multi-material flow with large fluid distortion", Numerical Methods for Fluid Dynamics, Academic, New York, 273-285, 1982
- Youngs D. L., "An interface tracking method for a 3D Eulerian hydrodynamics code" Technical Report 44/92/35, AWRE, 1984
- Youngs D.L., "Time-dependent multi-material flow with large fluid distortion." In K. W. Morton and M. J. Baines, editors, *Numerical Methods for Fluid Dynamics*. Academic Press, New York, 1992

- Zappa C. J. "Microscale wave breaking and its effect on air-water gas transfer using infrared imagery" Ph.D. Thesis, Applied Physics Laboratory, University of Washington, Seattle, 1999
- Zappa C. J., Asher W. E. and Jessup A. T., "Microscale wave breaking and air-water gas transfer", *J. Geophys. Res.* **106**, 9385-9391, 2001
- Zappa C. J., Asher W. E., Jessup A. T., Klinke J. and Long S. R., "Microbreaking and the enhancement of air-water gas transfer velocities" *J. Geophys. Res.* **109**, No. C8, C08S16, 10-1029/2003JC0018002, 2004

## Appendix A

### Grid independent test

A grid independent test is conducted to find out the effect of grid size on the numerical simulation results. The different grid sizes used in the test are 1mm, 1.5mm, and 2mm at a wind speed of  $4.4\text{m}\cdot\text{s}^{-1}$ . Figure A.1 illustrates the effect of grid size on mean streamwise velocity near the water surface. The result shows no significant change of mean streamwise velocity when the grid size decreases from 2mm to 1mm. The mean streamwise velocity agrees well at the water surface and the depth within 15mm. There's slight difference at greater depth, but the maximum difference is no more than 6%. The average difference among them is 3%. Therefore, in order to save the running time in the numerical simulations, a grid size of 2mm is chosen throughout the study.

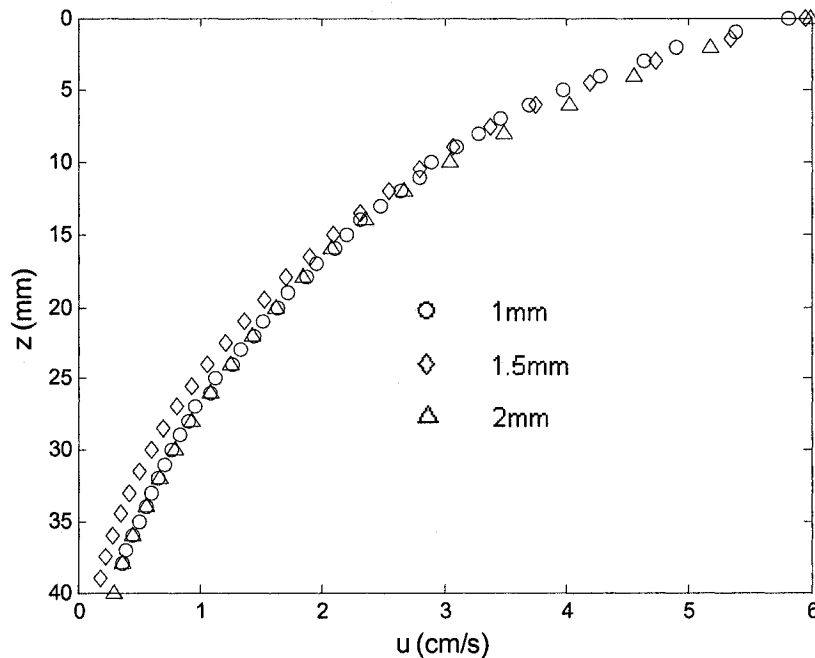


Figure A.1 The mean streamwise velocity for three different grid size at a wind speed of  $4.4\text{m}\cdot\text{s}^{-1}$ .